Neuronal apoptosis drives remodeling states of microglia and shifts in survival pathway dependence

Sarah R Anderson[1], Jacqueline M Roberts[1], Nate Ghena[1,2], Emmalyn Irvin[1], Joon Schwakopf[1], Isabelle Cooperstein[1], Alejandra Bosco[1], and Monica L Vetter[1#]

1. Department of Neurobiology, University of Utah School of Medicine
2. Interdepartmental Program in Neuroscience, University of Utah

Corresponding author

Abstract:

Microglia serve critical remodeling roles that shape the developing nervous system, responding to the changing neural environment with phagocytosis or soluble factor secretion. Recent single-cell sequencing (scRNAseq) studies have revealed the context-dependent diversity in microglial properties and gene expression, but the cues promoting this diversity are not well defined. Here, we ask how interactions with apoptotic neurons shape microglial state, including lysosomal and lipid metabolism gene expression and independence from Colony-stimulating factor 1 receptor (CSF1R) for survival. Using early postnatal mouse retina, a CNS region undergoing significant developmental remodeling, we performed scRNAseq on microglia from mice that are wild-type, lack neuronal apoptosis (Bax KO), or are treated with CSF1R inhibitor (PLX3397). We find that interactions with apoptotic neurons drives multiple microglial remodeling states, subsets of which are resistant to CSF1R inhibition. We find that TAM receptor Mer and complement receptor 3 are required for clearance of apoptotic neurons, but that Mer does not drive expression of remodeling genes. We show TAM receptor Axl is negligible for phagocytosis or remodeling gene expression but is consequential for microglial survival in the absence of CSF1R signaling. Thus, interactions with apoptotic neurons shift microglia towards distinct remodeling states and through Axl, alters microglial dependence on survival pathway, CSF1R.

30 **Introduction:**

31 Microglia are parenchymal innate immune cells and vital remodelers of the central nervous
32 system (CNS) [1]. They have a myriad of critical functions during development, including
33 elimination of viable or dying cells [2]. Similar to other macrophages, microglia are extremely
34 attuned to changes in their neural niche [3-5] and rapidly respond by phagocytosis or secreting
35 soluble factors. Recent single-cell RNA sequencing (scRNAseq) has demonstrated that
36 microglia are particularly diverse during development [6, 7]. However, we still lack an
37 understanding of the drivers of this heterogeneity, including the impact of environmental cues or
38 the act of phagocytosis itself. Therefore, connecting microglial states to specific developmental
39 events and determining the pathways involved remains a central challenge.

40

41 One developmental process fundamental for nearly every organ in the body is apoptotic death
42 of excess or dysfunctional cells [8]. In the CNS, death of neurons and glia is an essential and
43 well-documented feature of development [9]. Efferocytosis, or the phagocytosis of apoptotic
44 cells, is a rapid and carefully orchestrated process designed to minimize damage to surrounding
45 cells [10, 11]. Largely mediated by microglia, efferocytosis is important for maintaining CNS
46 homeostasis not only in development but in aging and disease as well [12, 13]. The developing
47 mouse retina is an excellent CNS model system to link remodeling events such as efferocytosis
48 and microglial state and function [14]. During the postnatal period in the retina, as circuits are
49 being established, waves of neuronal death occur [15]. For example, retinal ganglion cells
50 (RGCs), the projection neurons connecting retina and brain, undergo a well-characterized
51 culling during the first postnatal week which is dependent on pro-apoptotic factor, Bcl-2-
52 associated X protein (Bax) [16]. An estimated ~50% of RGCs will undergo apoptosis and need
53 to be cleared [17, 18]. We previously found that neuronal death significantly influences microglia
54 properties in postnatal retina, resulting in a majority of microglia expressing a distinct gene
55 signature and showing independence from colony-stimulating factor 1 receptor (CSF1R)

signaling for survival [19]. Relative to adult microglia, homeostatic genes were reduced while genes associated with phagocytosis and lipid metabolism were increased, similar to aging and disease-associated microglia (DAM) [20-22], and to developmental microglia residing in postnatal white matter tracts (PAM) [7] or (ATM) [6] or CD11c microglia [23].

Consistent with either apoptotic cell recognition or phagocytosis playing a central role in driving this gene signature, microglia in disease states increase select DAM genes in response to apoptotic cells [22], and ATM/PAM populations in the white matter tract engulf oligodendrocyte precursor cells [7, 24]. In disease, the TREM2 receptor is partially required for acquisition of the DAM signature [21, 22], but not for the developmental signature in retina [19] or brain [7]. Thus, it remains unclear to what extent the process of phagocytosis is altering properties of developmental microglia or whether distinct recognition pathways are involved. Microglia, like other macrophages, can recognize and engulf apoptotic (or viable) cells via a variety of ligand-receptor systems including C1q/C3 to complement receptor 3 (CR3) and exposed phosphatidylserine (PtdSer) to TAM family of tyrosine kinase receptors Mer (gene Mertk) and Axl [25], but how these pathways mediate changes in microglia properties and responses is an active area of research.

Here, we ask how neuronal apoptosis drives key properties of developmental microglia such as CSF1R independence and expression of DAM/ATM/PAM-related genes, and test the role of phagocytosis and specific recognition pathways. Through scRNAseq on postnatal retinal microglia we find considerable transcriptional heterogeneity, with multiple distinct microglial populations expressing DAM/ATM/PAM-related, lysosomal, and lipid metabolism genes. We further show, by analyzing microglia from Bax knockout (KO) retinas, that exposure to dying neurons drives several of these states and that most are more resistant to CSF1R inhibition. We find that CR3 and Mer are required for clearance of dying RGCs, but not for augmenting

82 microglial survival in the absence of CSF1R signaling. Conversely, Axl is not required for
83 clearance of dying RGCs, but for mediating independence from CSF1R signaling for survival.
84 Loss of Mer did not have a widespread impact on expression of microglial remodeling genes,
85 and neither did loss of Axl or Mertk/Axl double KO (dKO), suggesting that TAM receptor-
86 mediated signaling or reduced clearance are not sufficient. Thus, we find that interactions with
87 apoptotic neurons drives developmental microglial diversity, and that distinct recognition
88 receptors mediate phagocytosis of dying cells versus specific microglial properties, including
89 microglial survival.
90
91 **Results:**
92 **Multiple microglial states coexist in postnatal retina**
93 To better understand the influence of environmental cues on microglial states, we first sought to
94 understand the extent of microglial heterogeneity in the postnatal retina and then explicitly
95 determine states that were driven by neuronal apoptosis. Second, we previously linked CSF1R
96 independence to a DAM/ATM/PAM-related signature and neuronal apoptosis [19], so we
97 wanted to identify and characterize microglial states that remained following CSF1R inhibition
98 (PLX3397, PLX). Therefore, we performed scRNAseq on sorted retinal microglia from 4 groups
99 at postnatal day 6 and 7 (P6/P7): Bax WT, Bax KO, CX3CR1-GFP/+ given vehicle (daily for 3
100 days), and CX3CR1-GFP/+ pups dosed with PLX3397 (daily for 3 days) (Figure 1A). Microglia
101 from Bax WT and littermate KOs ($CD45^+$ $CD11b^+$/CX3CR1-GFP^+ $CCR2^-$) as well as microglia
102 from PLX and vehicle controls ($CD45^+$ CX3CR1-GFP^+ $Ly6C^-$) were sorted (Supplemental 1A-D)
103 and sequenced using the 10X Genomics platform. Following sequencing and manual filtering
104 (Supplemental 2), we used in silico Bax genotyping to sort out and reassign a subset of cells
105 from animals incorrectly assigned to the Bax WT and KO groups (Supplemental 3).
106 Unsupervised clustering was performed on the 15,084 cells from the four groups (4,902 - Bax
107 WT; 4,224 - Bax KO; 4,198 - Vehicle; 1,760 - PLX3397) (Supplemental 4A). Of the 15,084 cells,

108 1,417 in satellite clusters were deemed non-microglia cells based on expression of established
109 markers and were excluded from further analysis (Supplemental 4B-E). Differences in cell
110 surface markers used to sort Bax WT/KO ($CD45^+CD11b^+CX3CR1^+CCR2^-$) compared to
111 PLX/Vehicle ($CD45^+CX3CR1^+Ly6C^-$) (Supplemental 1) led to variance in the proportion of
112 macrophage/monocyte-like cells (Supplemental 4F), but this had no major impact on microglial
113 cell number (Gray dots, Supplemental 4C,F).
114
115 Unsupervised re-clustering of 13,667 remaining cells yielded 11 microglia clusters (Figure 1B).
116 Cells from controls (Bax WT and Vehicle) were represented in every cluster (Figure 1C),
117 indicating that microglia in an individual developing CNS region during a specific time window
118 are strikingly diverse. Further, we found that Bax KO and PLX-treated microglia had dramatic
119 and opposing shifts in their distribution compared to controls (Figure 1C). To determine the
120 characteristics of the 11 clusters, we examined the top genes for each (Figure 1D,
121 Supplemental Table 1). While virtually every cell expressed *Apoe* and *Ctsd*, consistent with our
122 previous findings [19], both genes were significantly enriched in cluster 0, which had high
123 expression of other DAM/PAM/ATM genes such as *Lyz2* and *Cd9*, but also intermediate levels
124 of homeostatic gene expression such as *P2ry12* and *Tmem119*. Thus, we called this cluster
125 Apoe-enriched. Cluster 1 had highest expression of *Tmem119* and *P2ry12* as well as other
126 homeostatic genes, including *Itgam, Siglech, Tgfbr1, P2ry13, Selplg, and Adgrg1* and so we
127 named it Homeostatic. Cluster 2 was enriched for chemokines including *Ccl4* and *Ccl3,* two
128 genes previously found in injury-responsive microglia in demyelinated lesions [6] and in PAM of
129 developing WM tracts [7], and had intermediate/high expression of homeostatic genes (e.g.
130 *Tmem119*; Figure 1D) and so we termed it Hom/chemokine cluster. Since *Ccl3* and *Ccl4* can be
131 induced by dissociation [26] we confirmed expression of *Ccl3* by *in situ* hybridization in whole
132 mount retina (Supplemental 5). Cluster 3 was marked by *Npl*, found in lipid-droplet microglia
133 [27], and *Apoc1*, a lipoprotein high in MS-associated human microglia [28]. Since this cluster

134 was substantially increased in PLX-treated retinas, we named this cluster PLX-enriched.
135 Chemokines *Cxcl2* and *Cxcl10* and pro-inflammatory cytokines, such as *Il1b* and *Tnf,* were high
136 in Cluster 4, dubbed the Chemokine/cytokine cluster. Cluster 5 most resembled ATM [6] (43/68
137 genes shared) and PAM [7] (41/68 genes shared) with specific expression of *Spp1* and high
138 expression of *Fabp5, Ctsl, Lpl, Igf1,* and *Csf1* and thus we termed it ATM/PAM-like. Cluster 6,
139 was named Antioxidant-responsive cluster due to high expression of antioxidant responsive
140 genes, *Hmox1* and *Gclm* [29]. Clusters 7, 8, and 9 represented Cycling microglia and expressed
141 *Mki67, Top2a*, and *Mcm* genes. Cluster 10, the smallest, contained 71 cells with high and very
142 specific expression of interferon response genes *Ccl5, Ifit3* and *Ifitm3* [30] and was thus termed
143 Interferon-responsive cluster. Thus, these data suggest that within the developing retina,
144 several microglial states coexist including homeostatic and various subsets of DAM/PAM/ATM-
145 related and chemokine-expressing microglia.
146
147 **Postnatal retinal microglia encompass a spectrum of homeostatic to remodeling states**
148 We noted a continuum of expression of the homeostatic genes *Tmem119* and *P2ry12* across
149 the clusters that appeared to be inverse to broadly expressed DAM/PAM/ATM genes such as
150 *Apoe, Ctsd* (Figure 1D). We more closely examined the expression of homeostatic genes, as
151 well as genes associated with lysosomal function, lipid metabolism and transport, and other
152 DAM/PAM/ATM-related genes. As for *Tmem119* and *P2ry12*, we found a gradient of expression
153 of other homeostatic genes including *Siglech, Tgfbr1, Mafb* and *Selplg* which were highest in
154 Homeostatic cluster (1), high/intermediate in Hom/chemokine (2), intermediate in Apoe-enriched
155 (0), Chemokine/cytokine cluster (4), ATM/PAM-like (5), and Antioxidant-responsive (6), with
156 lowest expression in PLX-enriched cluster (3), suggesting a spectrum from more to less
157 homeostatic (Figure 2B).
158

159 To determine whether this related to shifting phagocytic function of microglia, we examined the
160 expression of lysosomal genes *Cst7, Lyz2, Galns* and *Ctsb* and saw roughly the opposite
161 pattern. These genes were either absent or sparse in Homeostatic cluster (1) and
162 Hom/chemokine (2) and more highly expressed in Apoe-enriched (0), PLX-enriched (3),
163 Chemokine/cytokine cluster (4), ATM/PAM-like (5), and Antioxidant-responsive (6) (Figure 2C).
164 Notably, *Lyz2* showed highest levels in PLX-enriched (3) the least homeostatic cluster.
165 Additionally, genes involved with lipid metabolism and cholesterol transport, important
166 processes following the engulfment of apoptotic cells [31], followed the same trend (Figure 2D).
167 Thus, microglia in clusters (0,3,4,5 and 6) are equipped to be actively breaking down
168 phagocytosed material compared to more homeostatic clusters (1,2). Therefore, we conclude
169 that clusters 0,3,4,5, and 6 are involved in active remodeling activities and will refer to them as
170 remodeling clusters (Figure 2A). Since we saw enrichment of *Apoe* and *Ctsd* in these
171 remodeling clusters, we examined the expression of additional DAM/ATM/PAM-related genes,
172 including *Cd9, Igf1*, as well as the recognition receptors *Itgax* and *Axl*. We noted similar low
173 expression in Homeostatic cluster (1) and Hom/chemokine (2) and high expression in the
174 remodeling clusters (0,3,4,5,6) (Figure 2E). Interestingly, DAM/PAM/ATM-related genes had
175 varying cluster specificity. Genes such as *Apoe* were expressed in nearly every cell, whereas
176 *Igf1* and *Spp1* were more restricted to specific clusters, suggesting that regulation of these
177 genes is complex (Figure 1D, 2E). Together, these results suggest that phagolysosomal
178 function defines the spectrum of microglial states in the postnatal retina.
179

180 **Neuronal apoptosis drives multiple remodeling states**

181 We previously showed that neuronal death has a major influence on expression of remodeling
182 genes in postnatal retinal microglia [19] and wondered whether recognition or clearance of dying
183 neurons was a key factor in driving diverse microglial remodeling states. We examined microglia
184 from Bax KO retinas in which apoptotic death programs in RGCs and other neurons are

185 selectively lost [32] and saw a dramatic shift in cluster distribution with the loss of Bax compared
186 to littermate controls (Figure 3A). We found a 5-fold expansion in the Homeostatic cluster (1) in
187 Bax KO compared to WT (Figure 3A,B,C). This was concurrent with decreases in remodeling
188 clusters Apoe-enriched (0), Chemokine/cytokine expressing (4), and ATM/PAM-like (5), and the
189 minor PLX-enriched cluster (3), which were 4.7-fold, 3.46-fold, 5.86-fold, and 5-fold more
190 abundant in WT, respectively (Figure 3A,B). Clusters that remained largely unaltered included
191 Hom/chemokine (2), Antioxidant-responsive (6), Cycling (7-9), and Interferon-responsive (10),
192 suggesting they were not driven by apoptotic cell interactions or clearance (Figure 3A,B).
193 Therefore, we conclude that the spectrum of homeostatic to more remodeling clusters (0,3,4
194 and 5) in the postnatal retina is driven predominately by neuronal apoptosis.
195
196 To further examine microglial genes dependent on neuronal apoptosis, we compared all cells
197 from each genotype, ignoring cluster membership, and identified genes that were specific to
198 each sample (Figure 3D, Supplemental Table 2). Consistent with a shift to a more homeostatic
199 state, *Tmem119, P2ry12*, and *Siglech* were among the 133 upregulated genes in microglia from
200 Bax KO retina. The 183 downregulated genes included lysosomal and lipid metabolism genes
201 such as *Apoe, Lyz2, Cst7, Ctsb, Lpl*, and *Cd68,* DAM/PAM/ATM-related genes such as *Igf1* and
202 *Spp1,* and recognition receptors *Itgax* and *Axl* (Figure 3C,D). We next performed KEGG
203 analysis using GeneCodis 4 [33] on downregulated genes in Bax KO to identify major pathways
204 driven by interactions with dying neurons (Figure 3E). Consistent with the idea that microglial
205 phagocytosis was a key factor in these gene expression changes, we found metabolic and
206 lysosomal pathways significantly reduced. To determine whether loss of Bax altered microglia
207 density or distribution, we used C1q as a marker for microglia, which we validated by both
208 scRNAseq (Supplemental 4C) and immunostaining (Supplemental 7A,B). We found that
209 microglia remained uniformly spaced but that density was reduced by nearly half in Bax KO
210 retinas (Supplemental 7C,D), consistent with our prior flow cytometry analysis [19]. Altogether,

211 this suggests that neuronal apoptosis regulates important properties of microglia in the postnatal
212 retina, including overall density as well as the emergence of multiple remodeling states.
213
214 **Subsets of remodeling states survive CSF1R inhibition, while homeostatic microglia are**
215 **more vulnerable**
216 A striking property of microglia in postnatal retina is that ~60% survive inhibition of CSF1R
217 signaling [19], while only very small subsets show this property in adult brain [34]. We previously
218 found that surviving microglia had reduced homeostatic gene expression and increased
219 DAM/PAM/ATM gene expression, and this required neuronal apoptosis [19]. Since we found
220 that the less homeostatic remodeling clusters (0,3,4,5) were driven by neuronal apoptosis, we
221 investigated whether these microglial states would be more resistant to CSF1R inhibition. We
222 examined scRNAseq of Vehicle and PLX-treated microglia (dosed for three days) and found a
223 large shift in the distribution of cells across clusters with PLX treatment (Figure 4A). Several
224 remodeling clusters were either enriched or maintained. The least homeostatic cluster, PLX-
225 enriched (3), which was a very small proportion of cells in both Vehicle and Bax WT (Figure
226 3A,B), represented nearly 60% of remaining microglia following PLX3397 (increased 60-fold)
227 and thus seemed to arise, in part, by treatment (Figure 4A,B). This could potentially be due to
228 the further reduction of homeostatic properties of surviving microglia with CSF1R blockade [35].
229 Remodeling cluster Chemokine/cytokine (4) was increased 2-fold with PLX-treatment and
230 ATM/PAM-like (5), Antioxidant-responsive (6), and Interferon-responsive (10) were slightly
231 reduced or unchanged (0.755-fold, 0.654-fold, 0.979-fold, respectively), suggesting they are
232 more resistant than other subsets (Figure 4A,B). Conversely, we found clusters that had high or
233 intermediate expression of homeostatic genes, Apoe-enriched (0), Homeostatic (1),
234 Hom/chemokine (2), and Cycling (7,8,9) were largely absent following PLX treatment,
235 suggesting these clusters are more dependent on CSF1R for survival or that they had shifted to
236 a different state (Figure 4A,B). We noted the overlap between clusters dependent on neuronal

237 apoptosis (0,3,4 and 5) and resistant to loss of CSF1R signaling (3,4,5,6 and 10), illustrating the
238 link between the two and further arguing that certain microglial states driven by neuronal
239 apoptosis confer CSF1R independence. Furthermore, we found that downregulation of *Csf1r*
240 alone does confer independence as more resistant clusters (3,4,5 and 6) had slightly reduced
241 expression of *Csf1r* compared to susceptible clusters (0,1, and 2) but comparable to other
242 susceptible clusters (7,8,9) (Figure 4D), consistent with our previous findings [19].
243
244 To further probe genes and pathways enriched following CSF1R inhibition, we performed a
245 pairwise comparison on all Vehicle and PLX-treated cells, regardless of cluster. We found that
246 DAM/ATM/PAM-related genes *Apoe, Itgax,* and *Fabp5*, lysosomal genes *Lyz2* and *Ctss,* and
247 lipid metabolism genes *Nceh1*, *Soat1, Abca1,* and *Apoc1* were among the 254 upregulated
248 genes in PLX-treated cells (Figure 4C,E, Supplemental Table 3). Consistent with a loss of more
249 homeostatic microglia, homeostatic genes including *Tmem119, P2ry12,* and *Siglech* were
250 significantly reduced (181 genes downregulated) (Figure 4C,E). To uncover pathways
251 associated with CSF1R independence, we performed KEGG analysis [33] on all upregulated
252 genes in PLX cells and found that translation, metabolic pathways, and phagosome processes
253 were enriched (Figure 4F). This suggested that CSF1R independent microglia may be in an
254 altered metabolic state due to phagolysosomal processes. Altogether, we conclude that CSF1R-
255 independence is linked to increased phagocytosis, lysosomal function, and altered microglia
256 metabolic states, and that homeostatic microglia are more dependent on CSF1R signaling for
257 survival.
258
259 **Mer and CR3 are required for apoptotic RGC clearance**
260 To understand the role of apoptotic cell phagocytosis in promoting distinct microglial properties,
261 we sought to test whether recognition receptors were important both for driving microglial
262 remodeling states as well as CSF1R independence. We first wanted to confirm that microglia

263 were important for clearance of dying neurons within the retina and identify the recognition
264 receptors required, focusing on apoptotic RGCs. We performed a screen of genetic KO of
265 receptors previously implicated in the finding, recognition, or phagocytosis of apoptotic cells:
266 find-me pathway, fractalkine receptor CX3CR1 [36], integrin receptor complement receptor 3
267 (integrin $\alpha_M ß_2$, CD11b, CR3), TAM receptors Mer and Axl (Figure 5A) [25]. We used wildtype
268 animals from the CX3CR1 (CX3CR1-WT) and Mer (Mertk-WT) background as well as CX3CR1-
269 GFP/+ [37] for controls. First, we looked at whether loss of any of these receptors resulted in
270 changes to microglial density. By wholemount immunostaining, we found slight variations at P5
271 but none that reached significance compared to CX3CR1-GFP/+ (Supplemental Figure 8A,B).
272 Next, we analyzed the density of total apoptotic bodies by cleaved caspase 3 (CC3) in the
273 ganglion cell layer shortly after peak RGC death to measure any buildup or failure to clear
274 (Supplemental Figure 8C,D and Supplemental Figure 9A). We found that loss of CX3CR1, CR3,
275 Mer, and both Mer/Axl resulted in increased apoptotic body density compared to WT controls
276 suggesting these pathways were important for microglial phagocytosis of dying cells within the
277 retina. To ask what pathways were important for clearing dying RGCs specifically, we looked at
278 the density of $CC3^+RBPMS^+$ double-positive cells at P5 in all KOs (Figure 5B,C,D,
279 Supplemental Figure 9B). We found the CR3 KO, Mertk KO, and Mertk/Axl dKO all had
280 increased density of dying RGCs compared to controls (Figure 5B,C) with no change in overall
281 RGC density or retinal blood vessel development (Supplemental Figure 8E,F,G,H). CX3CR1
282 and Axl were dispensable for clearance of dying RGCs and Mertk/Axl dKOs did not appear to
283 have a further clearance deficit above Mertk KO alone (Figure 5B,C). Thus, both CR3 and Mer
284 receptors, which are broadly expressed in microglia, are important for the timely clearance of
285 RGCs undergoing developmental cell death, consistent with prior studies implicating these
286 pathways in efferocytosis in the CNS.
287
288 **<u>Axl promotes microglial survival in the absence of CSF1R signaling</u>**

289 Having identified receptors important for RGC clearance (CR3 and Mer), we were next able to
290 ask whether these pathways were also important for driving microglial survival following CSF1R
291 inhibition. We administered PLX3397 as previously published [19] (Figure 6A) and, surprisingly,
292 found that loss of CR3, CX3CR1, or Mer did not significantly reduce the proportion of surviving
293 microglia compared to controls (Figure 6B,C). However, loss of Axl allowed for greater
294 depletion, matching levels achieved with loss of developmental apoptosis (Bax KO) that we
295 previously reported [19] (Figure 6B,C). Mertk/Axl dKOs did not have an additive effect,
296 suggesting Axl signaling alone was important for microglial survival in the absence of CSF1R
297 signaling (Figure 6B,C). Altogether, we find that the receptors important for effective clearance
298 (Mer and CR3) do not alter microglial dependence on CSF1R, but that TAM receptor Axl, which
299 is induced by neuronal apoptosis, augments microglial survival in the absence of CSF1R
300 inhibition in retina.
301
302 **Mer and Axl are not required for expression of lysosomal, lipid metabolism, or**
303 **remodeling genes**
304 Since Mer was important for phagocytosis while Axl mediated survival in the absence of CSF1R
305 signaling, we wanted to delineate microglial gene expression changes that were driven by Mer
306 versus Axl. We performed bulk RNA-seq on sorted microglia from P4 Mertk and Axl KOs and
307 compared them to WT controls by DESeq2 (Figure 7A). Compared to WT controls, we found
308 modest changes in gene expression, with 42 downregulated genes and 44 upregulated genes in
309 Mertk KO microglia (Figure 7B,D, Supplemental Table 4). However, despite the fact that Mertk
310 KOs had reduced clearance of dying RGCs, there was no effect on lysosomal or lipid
311 metabolism genes. Further, DAM/ATM/PAM-related genes were also not significantly reduced,
312 but, in fact, *Csf1* and *Itgax* were significantly increased (Figure 7B,D).
313

314 Comparison of Axl KO to WT microglia revealed even fewer differentially expressed genes, with
315 no change in lysosomal, lipid metabolism, or DAM/ATM/PAM-related gene expression, except
316 the downregulation of *Spp1*, and no change in genes associated with survival pathways (Figure
317 7C,D, Supplemental Table 4). The majority of differentially expressed genes were different in
318 the two KOs (Figure 7D); however, sequencing of microglia from P7 Mertk/Axl dKO retinas
319 again revealed no change in lysosomal, lipid metabolism, or DAM/PAM/ATM-related genes
320 (Supplemental 10A,B, Supplemental Table 5). Based upon these findings, we first conclude that
321 while phagocytosis is altered in Mertk KOs, this is not sufficient to suppress expression of
322 remodeling genes, suggesting that Mer-mediated signaling does not strictly drive microglia
323 remodeling gene expression. Furthermore, while Axl facilitates microglia survival after CSF1R
324 inhibition, it is also not required to drive microglia remodeling gene expression, raising the
325 possibility that Axl itself, through recognition of apoptotic neurons, could be mediating survival.
326

327 **Discussion:**

328 scRNAseq has revealed that microglia in development and disease are transcriptionally diverse
329 across the CNS [38]. Due to their remarkable plasticity, a major challenge is to determine the
330 impact of local cues on microglial state and properties. Here, using the postnatal retina as a
331 model system, we establish neuronal cell death as a key factor driving developmental microglia
332 diversity. We show by scRNAseq that multiple microglial states coexist within this discrete CNS
333 region, encompassing a spectrum from homeostatic to remodeling states with high lysosomal
334 and lipid metabolism gene expression. We establish that multiple distinct remodeling states are
335 driven by neuronal apoptosis, and further show that several of these remodeling states survive
336 CSF1R inhibition, while more homeostatic microglia are susceptible. CR3 and Mer are important
337 for clearance of apoptotic retinal neurons, while Axl facilitates microglial survival following
338 inhibition CSF1R, but neither significantly regulates expression of microglial remodeling genes.

339 Thus, we conclude that cell death is a critical cue for driving diverse microglial properties and
340 that multiple pathways contribute.
341
342 We identify several states of remodeling microglia characterized by reduced homeostatic gene
343 expression and elevated lipid metabolism and lysosomal genes, with more discrete expression
344 of various genes including chemokines/cytokines. Many of the genes in these remodeling states
345 are shared with microglia in developing white matter tracts of the brain (CD11c/ATM/PAM) [6, 7,
346 39] and disease (DAM) [20-22]. Unlike in brain, we find they represent a majority of microglia in
347 the early postnatal retina, with most of them dependent upon neuronal apoptosis. Due to the
348 large proportion of microglia expressing these remodeling genes, we broaden our
349 understanding of microglia subsets present during normal development. For example, we find
350 genes such as *Apoe* and *Ctsd* are widely expressed at varying levels, while *Fabp5* and *Spp1*
351 are confined to more discrete subsets, suggesting that regulation of these genes and microglial
352 states is multifaceted. At present, it remains unclear whether they transition from state to state.
353 Since we find an increase in the proportion of homeostatic microglia in Bax KO retinas, this
354 argues that microglia in the context of neuronal death shift from a homeostatic state to more
355 remodeling ones.
356
357 In other contexts, efferocytosis can have a major impact on the transcriptional profile and state
358 of the phagocyte. For example, phagocytosis promotes distinct transcriptional states in
359 macrophages in a tissue-specific manner throughout the body [40], and tissue macrophages
360 modify their repertoire of phagocytic machinery in response to phagocytosis [41]. In the CNS,
361 there is much to learn about how phagocytosis impacts microglial state and function [13, 42].
362 One study addressing this found engulfment of newborn neurons by microglia in adult
363 neurogenic zones stimulates a microglial secretome that subsequently regulates neurogenesis
364 [43]. Here, in the postnatal retina, phagocytosis and digestion appear to be a major aspect of

365 microglial heterogeneity. We postulate that some remodeling states may even represent distinct
366 stages of the clearance process. Our analysis also identified microglial states that are not
367 regulated by neuronal death, arguing they may be involved in other important microglial
368 functions during postnatal retinal development. For example, astrocytes are also pruned by
369 microglia in the postnatal retina, which has been shown to be Bax-independent and also not
370 require CR3, Mer, or CX3CR1 pathways [44]. Future studies could target these specific
371 microglia subsets and link them to other important remodeling functions in the developing retina.
372
373 Despite the fact that postnatal RGC death has been a well-characterized model of
374 developmental cell death of the CNS [16], the recognition pathways required for the clearance
375 of apoptotic RGCs was previously undefined. CR3 and Mer are well-known recognition
376 receptors in the clearance of stressed or dying neurons in various contexts [25]. Here, we show
377 that both receptors are important for clearance of apoptotic RGCs. Previous work has
378 suggested that complement component C1q may get deposited on exposed PtdSer [45],
379 suggesting the pathways might work together to signal for phagocytosis, but whether
380 complement and TAM pathways are working redundantly or cooperatively is unknown in any
381 context. While receptors Mer and Axl are both members of the TAM receptor family of tyrosine
382 kinases [46], it has been appreciated that Mertk is more stably expressed in microglia, while Axl
383 is more dynamic and upregulated with inflammation or disease [47]. Both have previously been
384 implicated in phagocytosis and in regulating inflammatory responses [48], however this is cell
385 type-dependent [49]. Here, we find Mertk/Axl dKO did not have an enhanced clearance deficit
386 for apoptotic RGCs compared to Mertk KO, although this could be due to a plateau effect since
387 RBPMS likely gets downregulated as apoptotic programs continue [50].
388
389 Although Mer is important for clearance, we did not see a dramatic reduction in lysosomal or
390 lipid metabolism genes in either Mertk or Axl KO microglia. These results are consistent with

391 disease contexts where loss of Mertk and Axl do not have a dramatic effect on the DAM
392 signature in mouse model of Alzheimer's disease [51]. This suggests that transcriptional
393 changes in postnatal retinal microglia may depend upon other pathways for apoptotic cell
394 recognition. An alternate possibility is that Mertk KO microglia are still clearing, but at a reduced
395 rate, since live-imaging has shown that loss of Mer results in delayed engagement with
396 apoptotic cells but does not abolish phagocytosis completely [52].
397
398 We previously found that a large proportion of microglia in the postnatal retina were more
399 resistant to inhibition of the important survival pathway CSF1R [19]. Here, we identify specific
400 remodeling states of microglia that persist following CSF1R inhibition showing reduced
401 homeostatic gene expression. Other groups recently found small populations of CSF1R-
402 independent or repopulating microglia in the brain, and we note similar patterns of gene
403 expression, with reduced homeostatic genes such as *Tmem119* and *P2ry12*, and increased
404 expression of genes such as *Lyz2* [34, 53]. In these microglia repopulation studies, it was
405 proposed that more immature microglia survive CSF1R inhibition, but microglia maturation may
406 not be a key factor in the context of development since we previously found greater dependence
407 of retinal microglia on CSF1R at embryonic stages than in postnatal retina [19]. We find that
408 most of these resistant microglia subsets are induced by neuronal apoptosis, consistent with our
409 prior analysis showing increased microglial dependence on CSF1R in Bax KO retina [19].
410 Interestingly, in culture, peritoneal and bone marrow macrophages that phagocytose apoptotic
411 cells also survive in the absence of serum or survival factors [54]. In periods of elevated cell
412 death and possible lack of extrinsic survival factors, such as neuronally expressed CSF1R
413 ligand, IL-34 [55], phagocytes such as microglia might have evolved strategies to survive in
414 order to continue their job of maintaining homeostasis or reducing inflammation [54].
415 Importantly, cholesterol, along with CSF-1/IL-34 and TGF-ß2, has been shown to be an
416 important survival factor for microglia in culture [56]. We observed that PLX-treatment resulted

417 in enrichment of microglia with the lowest levels of homeostatic gene expression and high levels
418 of lysosomal and lipid metabolism genes. Thus, CSF1R signaling may also be important for
419 promoting microglial homeostasis [57]. Consistent with this, mutations in CSF1R can lead to
420 leukoencephalopathy, a neurodegenerative disorder which is associated with loss of
421 homeostatic microglia phenotype [35]. It will be valuable for future studies to explore the
422 contributions of CSF1R signaling to microglial survival and homeostasis during development.
423
424 Here, we find that Axl expression, which is regulated by neuronal apoptosis, enhances
425 microglial survival in the absence of CSF1R signaling. Since loss of Axl did not substantially
426 alter expression of other candidate apoptotic or survival pathways in microglia, one possibility is
427 that signaling directly downstream of Axl is involved. Axl has been shown to inhibit apoptosis in
428 a variety of cell types [58] including fibroblasts [59], oligodendrocytes in contexts of growth
429 factor withdrawal or TNF toxicity [60], and in Gonadotropin-releasing hormone neurons in the
430 brain [61]. Its role in various types of cancer has been well-established for promoting tumor
431 growth and metastasis in part due to its ability to inhibit apoptosis of cancer cells [62]. Axl has
432 diverse downstream signaling cascades depending on context [58], but one candidate signaling
433 cascade is the PI3K-Akt-NfkB-Bcl2 pathway. Activation of PI3K and Akt has shown to be
434 important for survival of cultured macrophages [54], oligodendrocytes [60, 63], neurons [61] as
435 well as cancer cells [58].
436
437 Altogether, we show neuronal cell death is a key factor driving multiple states of microglia in
438 developing retina, with distinct transcriptional profiles and independence from CSF1R signaling
439 for survival. Apoptotic cell recognition by microglia is thus a critical developmental event driving
440 diverse effects on gene expression, clearance and survival, with distinct pathways involved in
441 mediating each of these responses.
442

Acknowledgements:

This research was supported by the National Eye Institute and the National Institute of Neurological Disorders and Stroke of the National Institutes of Health under Awards R01EY030307 (MLV), and T32EY024234, T32NS115664 (NG). We thank the University of Utah BPRB Animal Facility, University of Utah Flow Cytometry Core, University of Utah High Throughput Genomics Core, and University of Utah Bioinformatics Core for technical support.

449 **Materials and Methods:**

450 **Experimental Model and Subject Details**

451

452 Animal husbandry and procedures

453 All animals were treated within the guidelines of the University of Utah Institutional Animal Care
454 and Use Committee (IACUC) and all experiments were IACUC approved. Mice were housed in
455 an AAALAC accredited animal facility with 12h light/12h dark cycles and ad libitum access to
456 food and water. Both sexes were used for all experiments. Information on the ages of mice used
457 for each experiment can be found in the figures/text. Pexidartinib (PLX3397) (AdooQ
458 BioScience A15520) was dissolved in corn oil (Sigma-Aldrich C8267) and 10% DMSO (Fisher
459 Scientific BP231) and administered to postnatal pups by daily intraperitoneal injection P3-P5 or
460 P4-P6 at 0.25 mg/g body weight. Mice were euthanized by isoflurane asphyxiation followed by
461 decapitation.

462

463 Mouse strains

464 The B6.CX3CR1-GFP/+ mice were a gift from Richard Lang with permission from Dr. Steffen
465 Jung [37]. Bax KO mice (JAX 002994) and B6. CD11b KO (JAX 003991) were purchased from
466 the Jackson Laboratory. The B6.Mertk KO and B6.Axl KO strains were a kind gift from Dr. Greg
467 Lemke.

468

469 **Method Details**

470 Tissue processing

471 Following euthanasia, retinas were dissected in ice-cold 0.1M PBS. Whole heads were fixed in
472 4% PFA for 45 minutes to an hour. Heads were washed 3 times for 15 minutes in PBS and
473 underwent 12-16-hour consecutive treatments with 15% and 30% sucrose in PBS at 4°C.
474 Heads were then embedded in OCT compound (Ted Pella 27050), stored at -80°C, and

475 sectioned at 16μm thickness. For retinal whole mounts, eyes were removed from the head and
476 retinas were carefully dissected from the rest of the eye (cornea, lens, RPE, hyaloid
477 vasculature, vitreous, ciliary body) in ice-cold PBS. Whole neural retinas were washed in PBS
478 for 10-20 minutes and then fixed in 4% PFA for 30-45 minutes at room temperature. For
479 RNAase-free dissections for qHCR or FACs, retinas were carefully dissected in RNase-free
480 conditions using ice-cold, sterile RNase-free PBS, removing all non-neural eye tissue (ciliary
481 body, pigmented epithelium, vitreous).
482
483 Immunohistochemistry
484 As previously done [19], frozen sections were incubated at 37°C for 30 minutes, post-fixed for
485 15 minutes in 4% PFA and washed in ice cold PBS for 3 times for 5 minutes. Then they were
486 blocked for 1 hour at room temperature (0.2% triton-X, 10% BSA, 10% normal donkey serum in
487 0.01M PBS), and incubated in primary antibody overnight at 4°C in (0.2% triton-X, 5% BSA in
488 0.01M PBS). The following day, sections were washed 3 times with PBS and incubated in
489 secondary antibodies (5% BSA in PBS) for 2 hours at room temperature, washed, and mounted
490 with Fluoroshield mounting medium with DAPI (MilliporeSigma F6057). For whole mount
491 immunostaining, retinas were incubated in primary antibody at 4°C for 2 days. Primary
492 antibodies used: goat GFP (abcam ab5450), rabbit C1q 1:1500 (abcam ab182451), rabbit active
493 caspase-3 1:500 (CC3) (BD Biosciences 559565), guinea pig RBPMS 1:1000 (MilliporeSigma
494 ABN1376MI), FITC IB4-lectin 1:400 (Sigma L9381). Secondary antibodies: 488 Donkey anti-
495 goat 1:400 (Invitrogen A11055), 555 Donkey anti-rabbit (Life Technologies A31572), and 647
496 Donkey anti-guinea pig (Jackson ImmunoResearch 706-605-148).
497
498 In situ hybridization chain reaction (HCR)
499 Wholemount retinas were fixed overnight in 4% PFA in 4°C. Retinas were washed and
500 dehydrated in methanol/PBS at 25%, 50%, 2 times 100% for 15 minutes each, stored in 100%

501 methanol overnight at 4°C and 20°C long term. *In situ* hybridization was performed as published
502 [64] using v3.0 reagents from Molecular Instruments (https://www.molecularinstruments.com).
503 Briefly, samples were rehydrated using (75% Methanol/25% PBST, 50% Methanol/50% PBST,
504 25%, Methanol/75% PBST, 2 times 100% PBST), treated with Proteinase K, and post fixed 20
505 minutes at room temperature in 4% PFA, and washed 3 times with PBST. Pre-hybridization was
506 performed in 30% probe hybridization buffer for 30 minutes at 37°C, and retinas were placed in
507 hybridization buffer at 37°C overnight. Retinas were washed, placed in amplification buffer for
508 30 minutes at room temperature. Separately, hairpins used for amplification were denatured at
509 95°C for 90 seconds and cooled to room temperature for 30 minutes. Retinas were placed in
510 amplification buffer with hairpins at room temperature in the dark overnight. Retinas were
511 washed, DAPI stained, and mounted on slides. Probes recognizing all known transcript variants
512 for each of Cx3cr1 and Ccl3 were generated by Molecular Instruments. For Cx3cr1-GFP
513 knockin mice, the fluorescent signal represents detection of Cx3cr1 mRNA by HCR and GFP
514 fluorescence which persists through the procedure.
515
516 Confocal Microscopy
517 Confocal images were acquired on an inverted Nikon A1R Confocal Microscope. Images were
518 acquired at 20X objective with a 3X digital zoom. Multi-points were stitched with a 10% overlap.
519 Images of retinal whole mounts were 144 multi-point images (on average) to obtain the entire
520 dorsal retina. Stacks through the Z plane were at 0.8μm steps of about ~13 μm thickness to
521 capture just the nerve fiber layer (NFL) and ganglion cell layer (GCL) at 0.2μm pixel resolution.
522 Whole mount retina images represent max projections of inner retina (NFL/GCL) from the
523 central retina (optic nerve) to the periphery (edge of retina). In cases of microglial quantification,
524 whole mount imaging and analysis spanned ~25μm thickness from NFL to inner plexiform layer
525 (IPL). Image acquisition settings were consistent across ages and genotypes.
526

527 Fluorescence-Activated Cell Sorting (FACS) and Flow Cytometry

528 Except for SC-sequencing, we pooled 2 retinas from an individual animal for each sample for
529 flow cytometry and FACs. Freshly dissected pure retinas were dissociated in PBS, 50 mM
530 HEPES, 0.05mg/ml DNase I (Sigma D4513), and 0.025 mg/ml Liberase (Sigma 5401119001)
531 for 35 minutes with intermediate trituration at 37°C. Cells were passed through a 70 µm nylon
532 cell strainer, washed with ice-cold staining buffer (1X PBS, 2% BSA, 0.1% sodium azide, 0.05%
533 EDTA), and red blood cells were lysed (eBioscience 00-4333-57). Cell counts were determined
534 using a cell counter (Invitrogen Countess) and Fc block (BD Biosciences 553142) was added at
535 2 µL per 10^6 cells. Antibodies were applied for 30 min on ice. Antibodies used: BV421 CD45
536 1:200 (BD Bioscience 563890), 488 CD11b 1:200 (CD45 (BD Bioscience 557672), PE CCR2
537 1:200 (R&D Systems FAB5538P), and APC Ly6C 1:200 (BD Bioscience 560595). Cells were
538 washed, pelleted, and resuspended in 500 µL staining buffer. FACS was performed using a BD
539 FACS Aria cell sorter at the University of Utah Flow Cytometry Core. Forward and side scatter
540 were used to eliminate debris, and both the width and area of the forward and side scatter was
541 used to discriminate singlets. For flow analysis, roughly 1 million singlet events (300,000 in rare
542 cases) were recorded for flow analysis using FlowJo software (Flowjo, LLC, Ashland, Oregon).
543

544 Single-cell RNA sequencing

545 13 animals/26 retinas were pooled for each of the Bax WT and littermate KO samples. 12
546 animals/24 retinas for PLX3397 CX3CR1-GFP/+ and 11 animals/22 retinas were pooled for
547 Vehicle CX3CR1-GFP/+ controls. FACs protocol was performed as normal, except pooling 6
548 retinas per tube during dissociation. $CD45^+$ $CD11b^+$/GFP^+ $CCR2^-$ cells were sorted for Bax
549 samples and $CD45^+GFP^+$ $Ly6C^-$ cells were sorted for PLX and Vehicle samples. Cells were
550 sorted using a 5 laser BD FACSAria with a 70µm nozzle at 55psi by the University of Utah Flow
551 Core into a cold, empty tube before library generation. 15,000 cells for each Bax sample and
552 7,000-10,000 cells for PLX and Vehicle were loaded onto 10X chip. Single-cell libraries were

553 generated with 10X Genomics Single Cell 3' Gene Expression Library Prep v3 reagents at the
554 University of Utah High Throughput Genomics core. The libraries were sequenced on a
555 NovaSeq 6000 to generate at least 200 million paired end reads of 150 bp per sample.
556
557 Analysis of Single-cell RNA-seq Data
558 Aligned reads to the mm10 reference from 10X genomics (version 3.0.0 from Ensembl 93) and
559 generated feature-barcode matrices using cellranger count v3.1.0 with expected-cells set to
560 5000. Filtered feature matrices from cellranger were further filtered with Seurat (v3.1.5) [65].
561 High-quality cells were selected by < 10% mitochondrial gene content, and high number of
562 features (genes). Feature cut-off was specific to each sample: > 1,000 for Bax-ko, > 1,500 for
563 Bax-wt, > 1,800 for vehicle, and > 2,500 for PLX-treated. Likely doublets, with high transcript
564 counts, were also eliminated: < 25,000 counts for Bax-ko, < 27,000 for Bax-wt, < 47,000 for
565 vehicle, and < 125,000 for PLX treated. In silico genotyping, as described below, was used to
566 assign cells to the correct groups. Filtered cells from all samples were then merged and
567 processed with the SCTransform pipeline [66]. Mitochondrial percentage was regressed out of
568 the model and Bax, Ftl1, and Ftl1-ps1 were excluded from the variable features list used for
569 dimensionality reduction. From here we subsetted the data to include only microglial cells. We
570 identified non-microglia populations by their expression of Ptprc, Plac8, Clec12a, Ms4a7, Mrc1,
571 and Rorb, and reran the SCTransform pipeline as before with the exception that FindClusters
572 was run with resolution set to 0.5. Differentially expressed genes for cluster comparisons and
573 whole-sample comparisons were identified with the FindMarkers function, using default
574 parameters.
575
576 In Silico Genotyping
577 During single-cell library preparation, a portion of Bax-wt and Bax-ko cells were allocated to the
578 wrong sample. We used the scSplit pipeline [67] to perform in silico genotyping and reassign

579 these cells to the correct sample. Beginning with the bam file for each sample generated by
580 cellranger, we used samtools view v1.8 [68] to exclude reads with mapping quality < 10, or
581 flagged as unmapped, not primary alignment, fails quality checks, PCR or optical duplicate, or
582 supplementary alignment. These filtered bam files were used to identify single nucleotide
583 polymorphisms (SNPs) with freebayes v1.3.1(https://arxiv.org/abs/1207.3907v2). Indels, MNPs,
584 and complex alleles were filtered from the input to the algorithm. Region was set to
585 chromosome 7, where Bax is located, minimum allele count was set to 2, use-best-n-alleles was
586 set to 2, and minimum base quality was set to 1. Vcffilter v1.0.1 [69] was used to exclude SNPs
587 with quality score <=30. We found that some crucial SNPs were identified in one sample and
588 not the other, so Bcftools merge v1.9 [68] was used to combine all SNPs into a single file.
589 ScSplit count v1.0.0 [67] was used to the combined SNPs to generate count matrices for the
590 filtered cell barcodes identified by cellranger, and scSplit run, with expected number of mixed
591 samples set to 1, genotyped the individual cells based on these matrices. We assigned Bax-ko
592 and Bax-wt genotypes to the cell populations based on Bax, Ftl1, and Ftl1-ps1 expression.
593
594 Bulk RNA sequencing
595 For P4 WT, Mertk KO, and Axl KO samples, CD11b$^+$ CD45$^+$ Ly6c$^-$ cells from one animal (2
596 retinas) were sorted directly into RLT buffer using a 4 laser BD FACSAria at the University of
597 Utah Flow Core and stored at -80°C. 2 samples were pooled prior to RNA isolation so that each
598 replicate was cells from 2 animals/4 retinas. WT samples had 5470, 6134, 7029 cells, Mertk KO
599 samples had 4245, 4038, and 8591 cells, and AXL KO samples had 5790, 5282, and 5071
600 cells. For P7 WT and Mertk/Axl dKO, CD11b$^+$ CD45$^+$ cells from one animal (2 retinas) were
601 sorted directly into RLT buffer (QIAGEN 79216) and stored at -80°C. P7 samples were not
602 pooled and thus represent 1 animal/2 retinas. For WT samples, 3783, 4083, and 4982 cells
603 were collected. For Mertk/Axl dKO samples, 2408, 2633, and 2388 cells were collected.

604 RNA from all samples was purified using the RNeasy Plus Micro kit (QIAGEN 74034). Total
605 RNA was hybridized with the NEBNext rRNA Depletion Solution human/mouse/rat (E6310L) to
606 substantially diminish cytoplasmic and mitochondrial rRNA from the samples. Stranded RNA
607 sequencing libraries were prepared as described using the NEBNext Ultra II RNA Library Prep
608 Kit for Illumina (E7770L). Purified libraries were qualified on an Agilent Technologies 2200
609 TapeStation using a D1000 ScreenTape assay (cat# 5067-5582 and 5067-5583). The molarity
610 of adapter-modified molecules was defined by quantitative PCR using the Kapa Biosystems
611 Kapa Library Quant Kit (cat#KK4824). Individual libraries were normalized to 10 nM, and equal
612 volumes were pooled in preparation for Illumina sequence analysis. Sequencing libraries were
613 chemically denatured and applied to an Illumina NovaSeq flow cell using the NovaSeq XP
614 workflow (20043131). Following transfer of the flowcell to an Illumina NovaSeq 6000
615 instrument, a 150 x 150 cycle paired end sequence run was performed using a NovaSeq 6000
616 S4 reagent Kit v1.5 (20028312). Samples were sequenced to a depth of 39-76 million reads.
617
618 Analysis of Bulk RNA-seq Data
619 Optical duplicates were removed with clumpify using BBmap v38.34 (https://jgi.doe.gov/data-
620 and-tools/bbtools/bb-tools-user-guide/bbmap-guide/) and default settings, then Illumina
621 adapters were trimmed with cutadapt v1.16 [70] using a minimum overlap of 6 and minimum
622 length of 20. Reference database was generated by STAR v2.7.9a [71] using mouse Ensembl
623 release 104 with overhang set to 124. Trimmed reads were aligned in two pass mode to
624 generate a BAM file, sorted by coordinates. Reads were assigned to the target with the largest
625 overlap, and uniquely aligned, reversely stranded reads were counted with featureCounts v1.6.3
626 [72]. Differentially expressed genes were identified from counts using DESeq2 v1.32.0 [73].
627 Features with fewer than 5 reads in every sample were eliminated before DESeq was run. rlog-
628 transformed values were used for sample visualizations.
629

630 **Quantification and Statistical Analysis**

631 Image analysis

632 All counts were blinded and manual, performed using Nikon Elements software (Melville, NY).
633 For double-positive $CC3^+RBPMS^+$ or single $RBPMS^+$ counts of retinal whole mounts, two ROIs
634 of roughly 0.4 mm^2 of central and periphery of dorsal retina were analyzed. Images were max
635 projected and roughly 13μm thick, spanning the NFL to the GCL. For $CC3^+$ density, the entire
636 dorsal leaf was analyzed, roughly 2-3 mm^2 again spanning the NFL to GCL only. See also
637 Figure S9. For microglial quantification, whole mount imaging and analysis spanned ~25μm
638 thickness from NFL to IPL and 0.5625 mm^2 of the central to mid-peripheral, vascularized retina
639 of the dorsal leaf.

640

641 Statistical Methods

642 Detailed statistical information can be found in the figure legends, including tests used, sample
643 size, and precision measures. All image and flow data were analyzed using Prism 9 software
644 (GraphPad, La Jolla, CA). All data were first tested for normality using four tests: Anderson-
645 Darling, D'Agostino & Pearson, Shapiro-Wilk, and Kolmogorov-Smirnov test. If any one test
646 failed, non-parametric tests were used: Mann-Whitney for pair-wise comparisons and Kruskal-
647 Wallis for comparisons of more than three samples. For all t-tests, we applied the Welch's
648 correction if the two samples had unequal variances determined by an F-test. We tested for
649 heteroscedasticity in groups of 3 or more by a Brown-Forsythe test. If not significantly different,
650 we ran an Ordinary one-way ANOVA with post-hoc Tukey's multiple comparison test. If the
651 standard deviations were significantly different between groups, we ran a Welch's ANOVA with
652 post-hoc Dunnett's T3 multiple comparison's test. For all data that is presented as the mean,
653 error bars indicate the standard error of the mean, SEM. We used a 95% confidence interval
654 and a p-value of < 0.05 for rejecting the null hypothesis.

655

656 **Data and Software Availability**

657 The sequence data reported in this publication have been deposited in NCBI's Gene Expression

658 Omnibus (GEO) Accession #: GSE192602.

659 **References:**
660

661 1. Prinz, M., et al., *Microglia and Central Nervous System-Associated Macrophages-From*
662 *Origin to Disease Modulation.* Annual review of immunology, 2021. **39**: p. 251-277.

663 2. Anderson, S.R. and M.L. Vetter, *Developmental roles of microglia: A window into*
664 *mechanisms of disease.* Dev Dyn, 2019. **248**(1): p. 98-117.

665 3. Bennett, F.C., et al., *A Combination of Ontogeny and CNS Environment Establishes*
666 *Microglial Identity.* Neuron, 2018. **98**(6): p. 1170-1183.e8.

667 4. Gosselin, D., et al., *An environment-dependent transcriptional network specifies human*
668 *microglia identity.* Science (New York, N.Y.), 2017. **356**(6344): p. eaal3222.

669 5. Lavin, Y., et al., *Tissue-resident macrophage enhancer landscapes are shaped by the*
670 *local microenvironment.* Cell, 2014. **159**(6): p. 1312-1326.

671 6. Hammond, T.R., et al., *Single-Cell RNA Sequencing of Microglia throughout the Mouse*
672 *Lifespan and in the Injured Brain Reveals Complex Cell-State Changes.* Immunity, 2019.
673 **50**(1): p. 253-271.e6.

674 7. Li, Q., et al., *Developmental Heterogeneity of Microglia and Brain Myeloid Cells*
675 *Revealed by Deep Single-Cell RNA Sequencing.* Neuron, 2019. **101**(2): p. 207-223.e10.

676 8. Jacobson, M.D., M. Weil, and M.C. Raff, *Programmed Cell Death in Animal*
677 *Development.* Cell, 1997. **88**(3): p. 347-354.

678 9. Oppenheim, R.W., *Cell death during development of the nervous system.* Annu Rev
679 Neurosci, 1991. **14**: p. 453-501.

680 10. Morioka, S., C. Maueröder, and K.S. Ravichandran, *Living on the Edge: Efferocytosis at*
681 *the Interface of Homeostasis and Pathology.* Immunity, 2019. **50**(5): p. 1149-1162.

682 11. Boada-Romero, E., et al., *The clearance of dead cells by efferocytosis.* Nature Reviews
683 Molecular Cell Biology, 2020. **21**(7): p. 398-414.

684 12. Galloway, D.A., et al., *Phagocytosis in the Brain: Homeostasis and Disease.* Frontiers in
685 Immunology, 2019. **10**(790).

686 13. VanRyzin, J.W., *Phagocytic microglia in development: Are they what they eat?* Brain,
687 Behavior, & Immunity - Health, 2021. **18**: p. 100373.

688 14. Li, F., D. Jiang, and M.A. Samuel, *Microglia in the developing retina.* Neural Dev, 2019.
689 **14**(1): p. 12.

690 15. Braunger, B.M., C. Demmer, and E.R. Tamm, *Programmed cell death during retinal*
691 *development of the mouse eye.* Adv Exp Med Biol, 2014. **801**: p. 9-13.

692 16. Péquignot, M.O., et al., *Major role of BAX in apoptosis during retinal development and in*
693 *establishment of a functional postnatal retina.* Dev Dyn, 2003. **228**(2): p. 231-8.

694 17. Farah, M.H. and S.S. Easter, Jr., *Cell birth and death in the mouse retinal ganglion cell*
695 *layer.* J Comp Neurol, 2005. **489**(1): p. 120-34.

18. Farah, M.H., *Neurogenesis and cell death in the ganglion cell layer of vertebrate retina.* Brain Res Rev, 2006. **52**(2): p. 264-74.

19. Anderson, S.R., et al., *Developmental Apoptosis Promotes a Disease-Related Gene Signature and Independence from CSF1R Signaling in Retinal Microglia.* Cell Rep, 2019. **27**(7): p. 2002-2013.e5.

20. Holtman, I.R., et al., *Induction of a common microglia gene expression signature by aging and neurodegenerative conditions: a co-expression meta-analysis.* Acta Neuropathol Commun, 2015. **3**: p. 31.

21. Keren-Shaul, H., et al., *A Unique Microglia Type Associated with Restricting Development of Alzheimer's Disease.* Cell, 2017. **169**(7): p. 1276-1290.e17.

22. Krasemann, S., et al., *The TREM2-APOE Pathway Drives the Transcriptional Phenotype of Dysfunctional Microglia in Neurodegenerative Diseases.* Immunity, 2017. **47**(3): p. 566-581.e9.

23. Benmamar-Badel, A., T. Owens, and A. Wlodarczyk, *Protective Microglial Subset in Development, Aging, and Disease: Lessons From Transcriptomic Studies.* Front Immunol, 2020. **11**: p. 430.

24. Nemes-Baran, A.D., D.R. White, and T.M. DeSilva, *Fractalkine-Dependent Microglial Pruning of Viable Oligodendrocyte Progenitor Cells Regulates Myelination.* Cell Reports, 2020. **32**(7): p. 108047.

25. Lemke, G., *How macrophages deal with death.* Nature Reviews Immunology, 2019. **19**(9): p. 539-549.

26. Marsh, S.E., et al., *Single Cell Sequencing Reveals Glial Specific Responses to Tissue Processing & Enzymatic Dissociation in Mice and Humans.* bioRxiv, 2020: p. 2020.12.03.408542.

27. Marschallinger, J., et al., *Lipid-droplet-accumulating microglia represent a dysfunctional and proinflammatory state in the aging brain.* Nature Neuroscience, 2020. **23**(2): p. 194-208.

28. Masuda, T., et al., *Spatial and temporal heterogeneity of mouse and human microglia at single-cell resolution.* Nature, 2019. **566**(7744): p. 388-392.

29. Rojo, A.I., et al., *Redox control of microglial function: molecular mechanisms and functional significance.* Antioxidants & redox signaling, 2014. **21**(12): p. 1766-1801.

30. Dorman, L.C., et al., *A type I interferon response defines a conserved microglial state required for effective phagocytosis.* bioRxiv, 2021: p. 2021.04.29.441889.

31. Doran, A.C., A. Yurdagul, and I. Tabas, *Efferocytosis in health and disease.* Nature Reviews Immunology, 2020. **20**(4): p. 254-267.

32. Fricker, M., et al., *Neuronal Cell Death.* Physiological Reviews, 2018. **98**(2): p. 813-880.

33. García-Moreno, A., et al., *GeneCodis 4: Expanding the modular enrichment analysis to regulatory elements.* bioRxiv, 2021: p. 2021.04.15.439962.

734 34. Zhan, L., et al., *A MAC2-positive progenitor-like microglial population is resistant to*
735 *CSF1R inhibition in adult mouse brain.* Elife, 2020. **9**.

736 35. Kempthorne, L., et al., *Loss of homeostatic microglial phenotype in CSF1R-related*
737 *Leukoencephalopathy.* Acta Neuropathologica Communications, 2020. **8**(1): p. 72.

738 36. Wolf, Y., et al., *Microglia, seen from the CX3CR1 angle.* Frontiers in cellular
739 neuroscience, 2013. **7**: p. 26-26.

740 37. Jung, S., et al., *Analysis of fractalkine receptor CX(3)CR1 function by targeted deletion*
741 *and green fluorescent protein reporter gene insertion.* Mol Cell Biol, 2000. **20**(11): p.
742 4106-14.

743 38. Masuda, T., et al., *Microglia Heterogeneity in the Single-Cell Era.* Cell Rep, 2020. **30**(5):
744 p. 1271-1281.

745 39. Wlodarczyk, A., et al., *A novel microglial subset plays a key role in myelinogenesis in*
746 *developing brain.* Embo j, 2017. **36**(22): p. 3292-3308.

747 40. A-Gonzalez, N., et al., *Phagocytosis imprints heterogeneity in tissue-resident*
748 *macrophages.* Journal of Experimental Medicine, 2017. **214**(5): p. 1281-1296.

749 41. Zent, C.S. and M.R. Elliott, *Maxed out macs: physiologic cell clearance as a function of*
750 *macrophage phagocytic capacity.* The FEBS journal, 2017. **284**(7): p. 1021-1039.

751 42. Márquez-Ropero, M., et al., *Microglial Corpse Clearance: Lessons From Macrophages.*
752 Frontiers in Immunology, 2020. **11**(506).

753 43. Diaz-Aparicio, I., et al., *Microglia Actively Remodel Adult Hippocampal Neurogenesis*
754 *through the Phagocytosis Secretome.* The Journal of Neuroscience, 2020. **40**(7): p.
755 1453-1482.

756 44. Puñal, V.M., et al., *Large-scale death of retinal astrocytes during normal development is*
757 *non-apoptotic and implemented by microglia.* PLOS Biology, 2019. **17**(10): p. e3000492.

758 45. Païdassi, H., et al., *C1q binds phosphatidylserine and likely acts as a multiligand-*
759 *bridging molecule in apoptotic cell recognition.* J Immunol, 2008. **180**(4): p. 2329-38.

760 46. Lemke, G., *Biology of the TAM receptors.* Cold Spring Harbor perspectives in biology,
761 2013. **5**(11): p. a009076-a009076.

762 47. Fourgeaud, L., et al., *TAM receptors regulate multiple features of microglial physiology.*
763 Nature, 2016. **532**(7598): p. 240-244.

764 48. Elliott, M.R., K.M. Koster, and P.S. Murphy, *Efferocytosis Signaling in the Regulation of*
765 *Macrophage Inflammatory Responses.* J Immunol, 2017. **198**(4): p. 1387-1394.

766 49. Seitz, H.M., et al., *Macrophages and Dendritic Cells Use Different Axl/Mertk/Tyro3*
767 *Receptors in Clearance of Apoptotic Cells.* The Journal of Immunology, 2007. **178**(9): p.
768 5635.

769 50. Elliott, Michael R. and Kodi S. Ravichandran, *The Dynamics of Apoptotic Cell Clearance.*
770 Developmental Cell, 2016. **38**(2): p. 147-160.

771 51. Huang, Y., et al., *Microglia use TAM receptors to detect and engulf amyloid β plaques.*
772 Nat Immunol, 2021. **22**(5): p. 586-594.

773 52. Damisah, E.C., et al., *Astrocytes and microglia play orchestrated roles and respect*
774 *phagocytic territories during neuronal corpse removal in vivo.* Sci Adv, 2020. **6**(26): p.
775 eaba3239.

776 53. Hohsfield, L.A., et al., *Subventricular zone/white matter microglia reconstitute the empty*
777 *adult microglial niche in a dynamic wave.* Elife, 2021. **10**.

778 54. Reddy, S.M., et al., *Phagocytosis of Apoptotic Cells by Macrophages Induces Novel*
779 *Signaling Events Leading to Cytokine-Independent Survival and Inhibition of*
780 *Proliferation: Activation of Akt and Inhibition of Extracellular Signal-Regulated Kinases 1*
781 *and 2.* The Journal of Immunology, 2002. **169**(2): p. 702.

782 55. Nandi, S., et al., *The CSF-1 receptor ligands IL-34 and CSF-1 exhibit distinct*
783 *developmental brain expression patterns and regulate neural progenitor cell*
784 *maintenance and maturation.* Dev Biol, 2012. **367**(2): p. 100-13.

785 56. Bohlen, C.J., et al., *Diverse Requirements for Microglial Survival, Specification, and*
786 *Function Revealed by Defined-Medium Cultures.* Neuron, 2017. **94**(4): p. 759-773.e8.

787 57. Hu, B., et al., *Insights Into the Role of CSF1R in the Central Nervous System and*
788 *Neurological Disorders.* Frontiers in Aging Neuroscience, 2021. **13**(807).

789 58. Axelrod, H. and K.J. Pienta, *Axl as a mediator of cellular growth and survival.*
790 Oncotarget, 2014. **5**(19): p. 8818-8852.

791 59. Goruppi, S., et al., *Requirement of phosphatidylinositol 3-kinase-dependent pathway and*
792 *Src for Gas6-Axl mitogenic and survival activities in NIH 3T3 fibroblasts.* Mol Cell Biol,
793 1997. **17**(8): p. 4442-53.

794 60. Shankar, S.L., et al., *Gas6/Axl signaling activates the phosphatidylinositol 3-kinase/Akt1*
795 *survival pathway to protect oligodendrocytes from tumor necrosis factor alpha-induced*
796 *apoptosis.* J Neurosci, 2006. **26**(21): p. 5638-48.

797 61. Pierce, A., et al., *Axl and Tyro3 Modulate Female Reproduction by Influencing*
798 *Gonadotropin-Releasing Hormone Neuron Survival and Migration.* Molecular
799 Endocrinology, 2008. **22**(11): p. 2481-2495.

800 62. Zhu, C., Y. Wei, and X. Wei, *AXL receptor tyrosine kinase as a promising anti-cancer*
801 *approach: functions, molecular mechanisms and clinical applications.* Molecular Cancer,
802 2019. **18**(1): p. 153.

803 63. Shankar, S.L., et al., *The growth arrest-specific gene product Gas6 promotes the*
804 *survival of human oligodendrocytes via a phosphatidylinositol 3-kinase-dependent*
805 *pathway.* J Neurosci, 2003. **23**(10): p. 4208-18.

806 64. Choi, H.M.T., et al., *Third-generation in situ hybridization chain reaction: multiplexed,*
807 *quantitative, sensitive, versatile, robust.* Development, 2018. **145**(12).

808 65. Stuart, T., et al., *Comprehensive Integration of Single-Cell Data.* Cell, 2019. **177**(7): p.
809 1888-1902.e21.

66. Hafemeister, C. and R. Satija, *Normalization and variance stabilization of single-cell RNA-seq data using regularized negative binomial regression.* Genome Biology, 2019. **20**(1): p. 296.

67. Xu, J., et al., *Genotype-free demultiplexing of pooled single-cell RNA-seq.* Genome Biology, 2019. **20**(1): p. 290.

68. Danecek, P., et al., *Twelve years of SAMtools and BCFtools.* Gigascience, 2021. **10**(2).

69. Garrison, E., et al., *Vcflib and tools for processing the VCF variant call format.* bioRxiv, 2021: p. 2021.05.21.445151.

70. Martin, M., *Cutadapt removes adapter sequences from high-throughput sequencing reads.* 2011, 2011. **17**(1): p. 3.

71. Dobin, A., et al., *STAR: ultrafast universal RNA-seq aligner.* Bioinformatics, 2013. **29**(1): p. 15-21.

72. Liao, Y., G.K. Smyth, and W. Shi, *featureCounts: an efficient general purpose program for assigning sequence reads to genomic features.* Bioinformatics, 2013. **30**(7): p. 923-930.

73. Love, M.I., W. Huber, and S. Anders, *Moderated estimation of fold change and dispersion for RNA-seq data with DESeq2.* Genome Biology, 2014. **15**(12): p. 550.

Supplement 1: Gating strategy to FAC-sort retinal microglia for single-cell sequencing

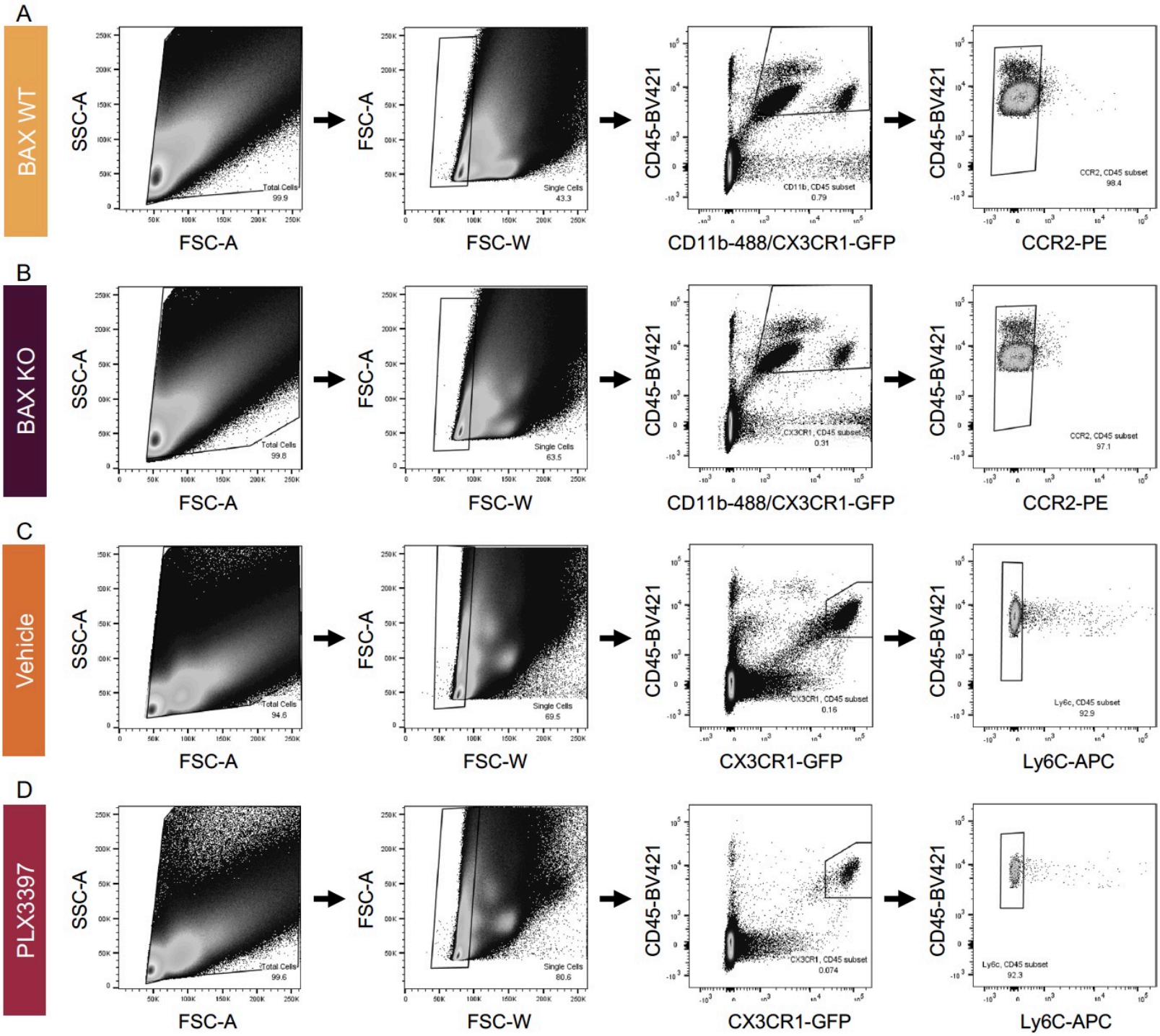

Figure S1. Related to Figure 1. (A) Gating strategy for FACs of BAX WT and (B) KO samples for single-cell sequencing. Animals were a mixture of CX3CR1-GFP/+ and CX3CR1-+/+. CCR2 was used to exclude monocytes and macrophages. (C) Gating strategy for FACs of CX3CR1-GFP/+ Vehicle and (D) PLX3397 treated samples. Ly6C was used to exclude monocytes and macrophages.

Supplement 2: Selection of high-quality cells

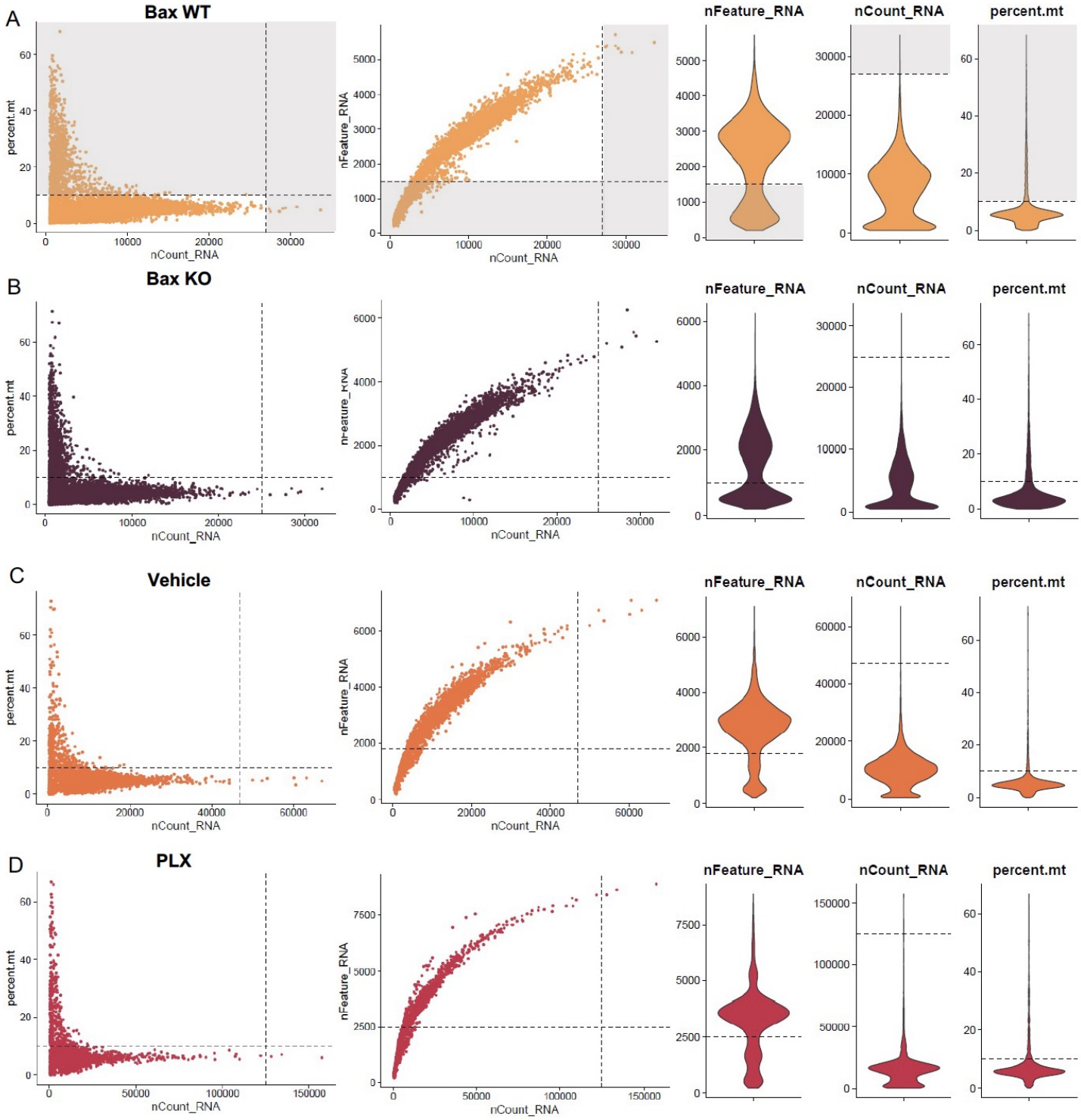

E

	Filtered by CellRanger				Manually filtered			
	# cells	Counts per cell	Genes per cell	Mito %	# cells	Counts per cell	Genes per cell	Mito %
Bax WT	7,499	7,532	2,241	7.36	5,237	9,922	2,845	5.24
Bax KO	7,072	4,359	1,531	6.66	3,889	7,012	2,290	3.68
Vehicle	5,117	10,271	2,696	5.84	4,198	11,876	3,056	4.77
PLX	2,437	15,777	3,186	7.90	1,760	20,011	3,862	5.61

Figure S2. Related to Figure 1. (A-D) Cells, as identified by CellRanger, were filtered to exclude low quality cells: those with few features (genes) or high mitochondrial content. Cells with especially high transcript counts were eliminated as potential doublets. Cut-offs were set independently for Bax WT (A), Bax KO (B), Vehicle (C), and PLX (D) samples. (E) Dataset composition before and after cell filtering.

Supplement 3: In silico *Bax* genotyping

A

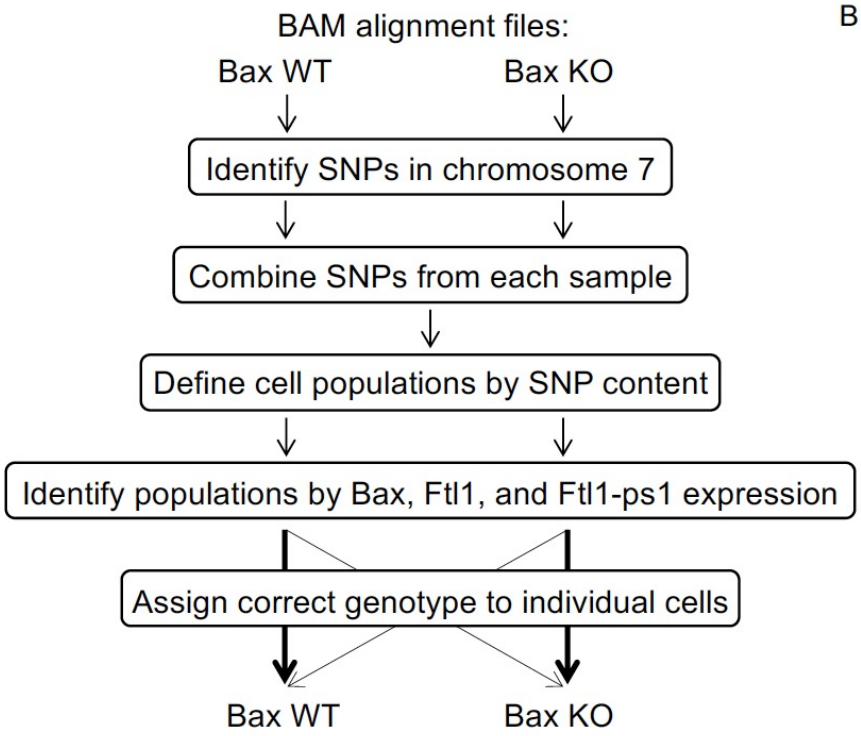

B

dataset	# wt cells	# ko cells
Bax WT	4,567	670
Bax KO	335	3,554

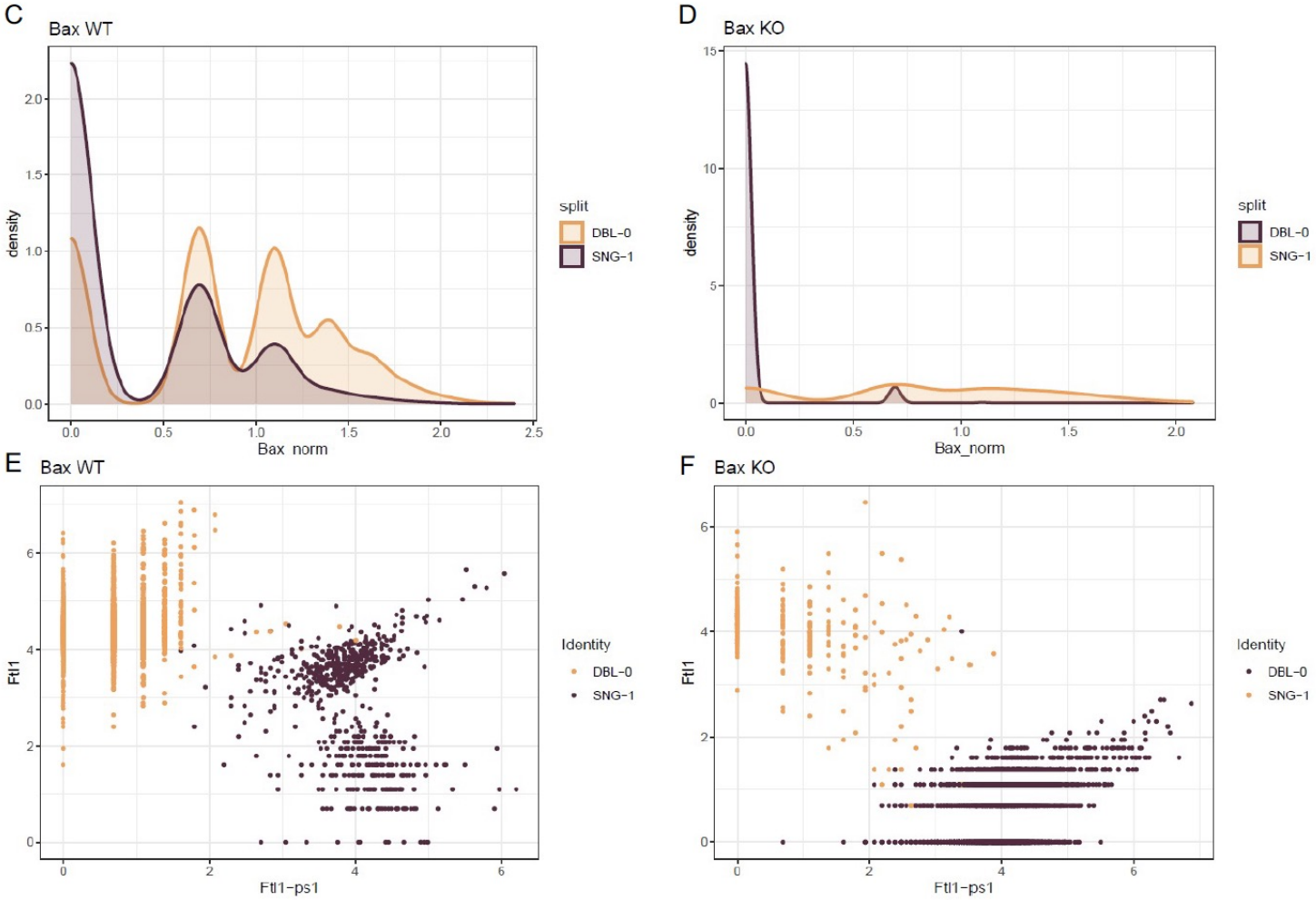

Figure S3. Related to Figure 1. (A) Summary of *in silico* genotyping workflow from alignment files to genotyping of individual cells. (B) Number of cells from the filtered dataset (Bax WT or Bax KO) ultimately assigned to each genotype (# wt or # ko). (C-F) In silico genotyping identified two populations within each dataset, which were classified as wt or ko based on (C, D) Bax, (E, F) Ftl1, and Ftl1-ps1 expression. Data shown are log normalized counts. The two populations are pseudocolored here: yellow for wt and purple for ko.

Supplement 4: Identification of non-microglia populations

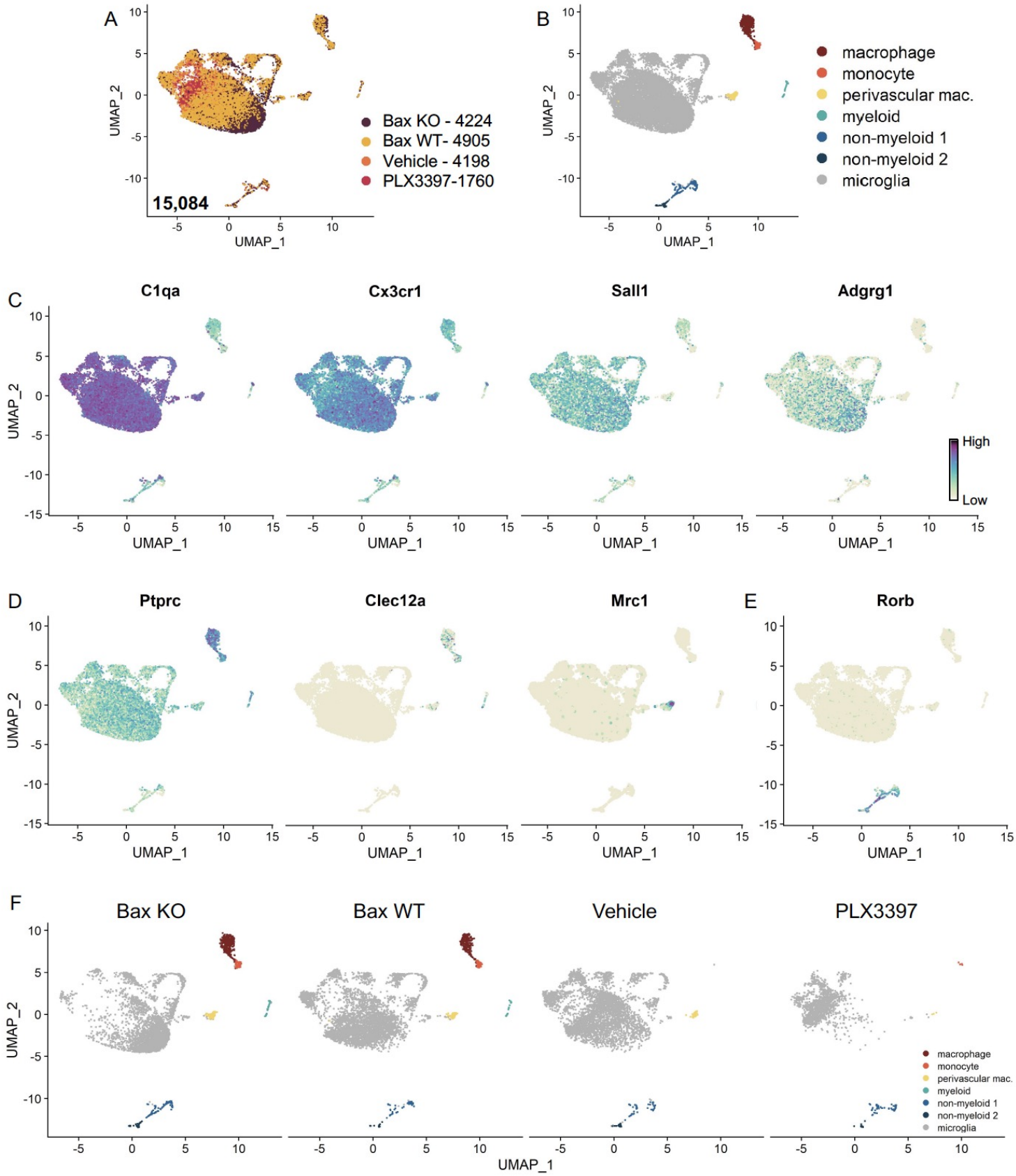

Figure S4. Related to Figure 1. (A) UMAP plot of 15,084 cells from all 4 samples. BAX KO, 4224 cells; BAX WT 4902 cells; Vehicle, 4198 cells; PLX3397, 1760 cells. (B) UMAP plot with clusters labeled based on published markers: macrophages (dark red), monocytes (bright red), perivascular macrophages (yellow), other myeloid-like cells (teal), non-myeloid 1 and 2 (shades of blue), and microglia (gray). (C) UMAP plots colored by relative gene expression (dark purple = highest, light yellow= lowest) of highly expressed or specific microglia genes. (D) UMAP plots of published monocyte or macrophage genes. (E) UMAP plot of neuronal gene expression. (F) UMAP plots illustrating the distribution of cells across clusters for each sample.

1. Multiple microglial states coexist in postnatal retina

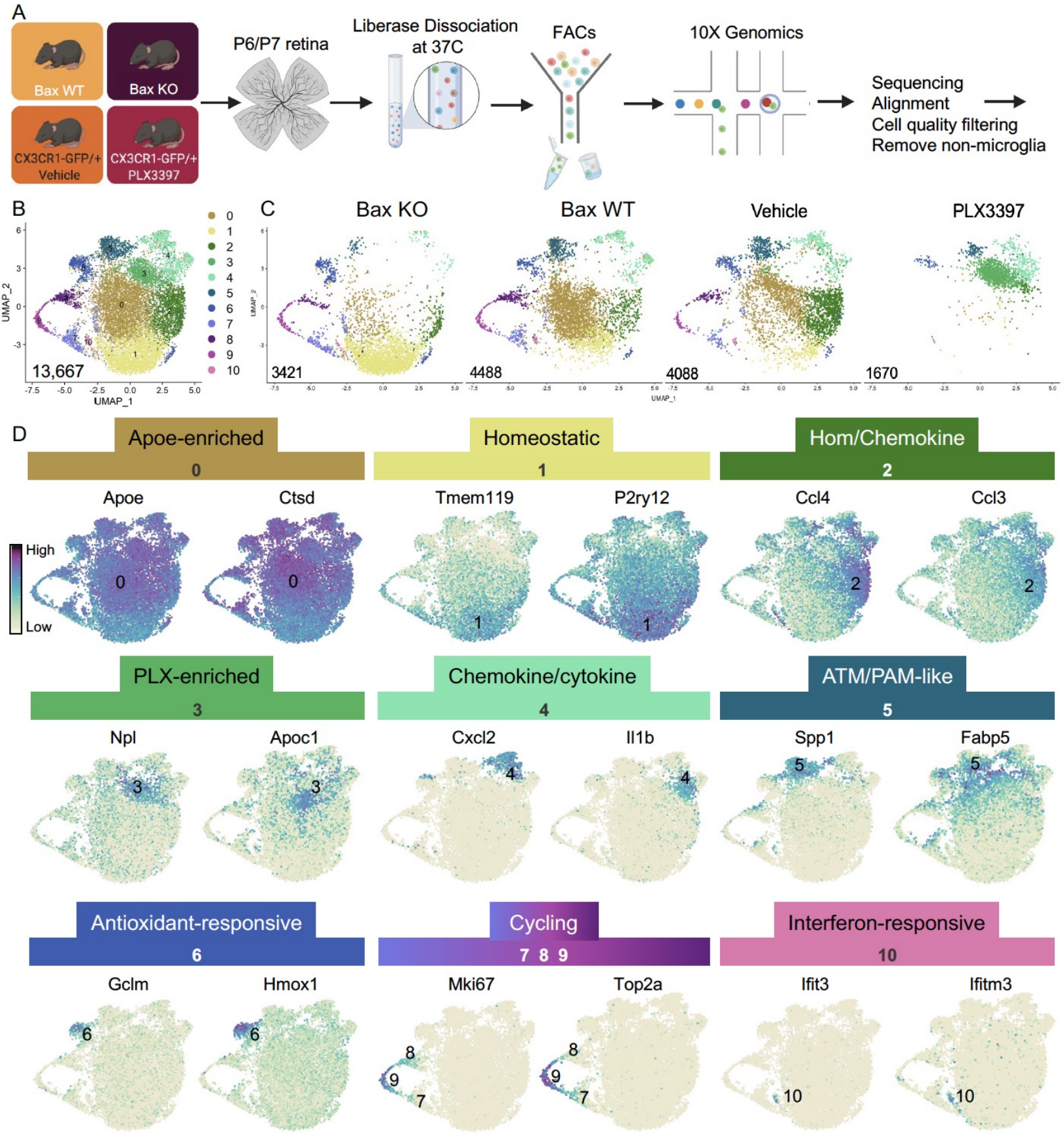

Figure 1. (A) Workflow for collection, dissociation, sorting, and sequencing of individual microglia from 4 different groups: Bax WT and KO, PLX and vehicle. (B) UMAP plot of 13,667 microglia cells from all 4 samples distributed into 11 clusters by unsupervised clustering. (C) UMAP plots illustrating the distribution of cells for each sample. Number of cells per sample labeled in lower left. (D) UMAP plots of two genes enriched in each cluster. Color scale is based on relative gene expression: dark purple = highest, light yellow = lowest.

Supplemental Fig 5. Postnatal retinal microglia express *Ccl3 in vivo*

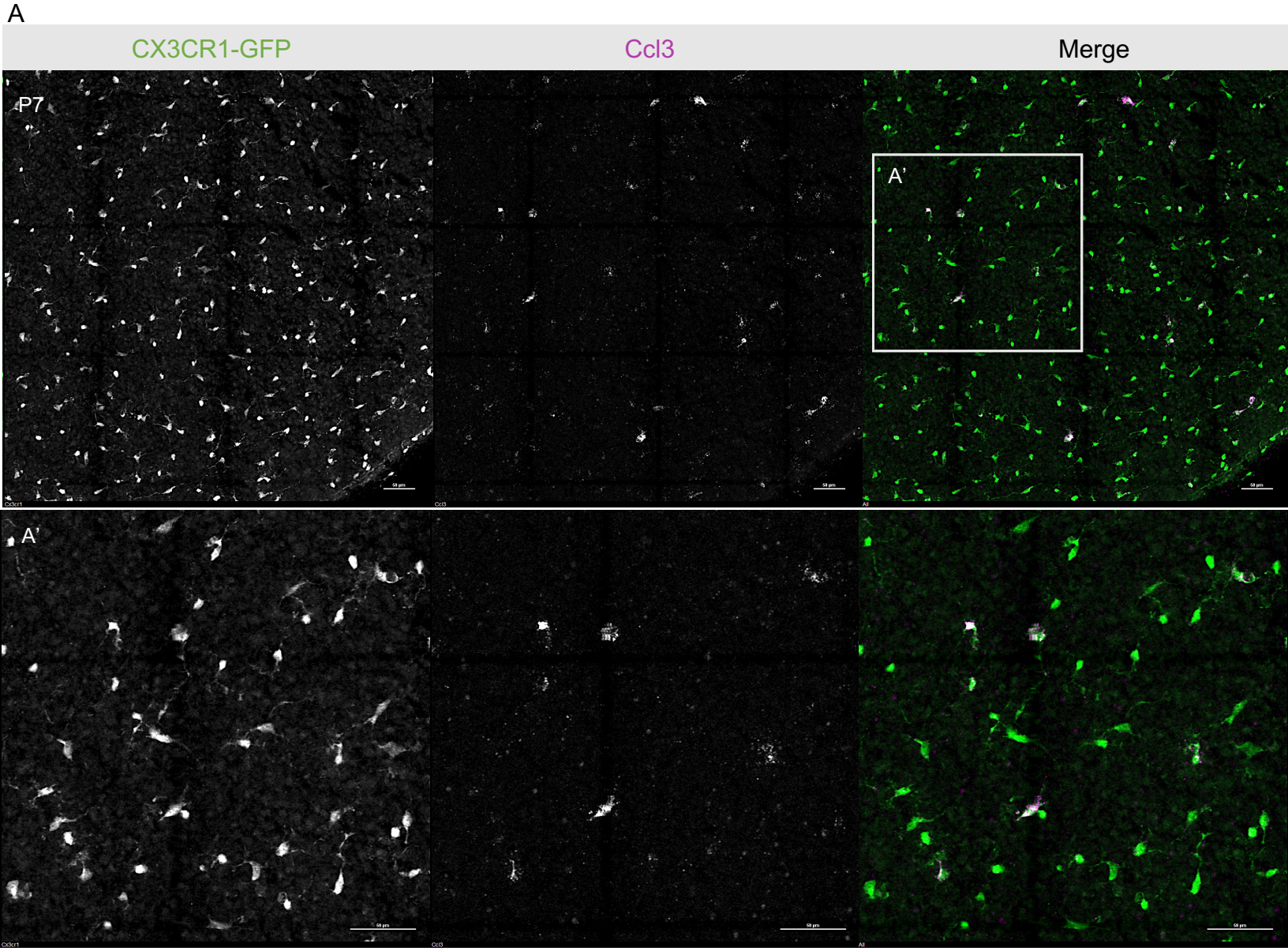

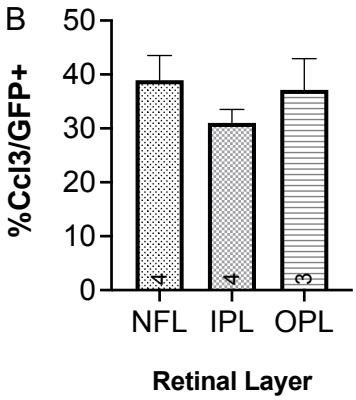

Figure S5. Related to Figure 1. (A) Max projected confocal image of *in situ* hybridization chain reaction (HCR) on P7 whole mount retina probed for *Ccl3*. CX3CR1-GFP (protein, green), Ccl3 (RNA, magenta). A' inset, higher magnification. Scale bar 50 µm (B) Percent *Ccl3*$^{+}$ of CX3CR1-GFP^{+} cells in each layer of the P7 retina of the mid-periphery. (n=>3; ±SEM). NFL, nerve fiber layer; IPL, inner plexiform layer; OPL, outer plexiform layer.

2. Postnatal retinal microglia encompass a spectrum of homeostatic to remodeling states

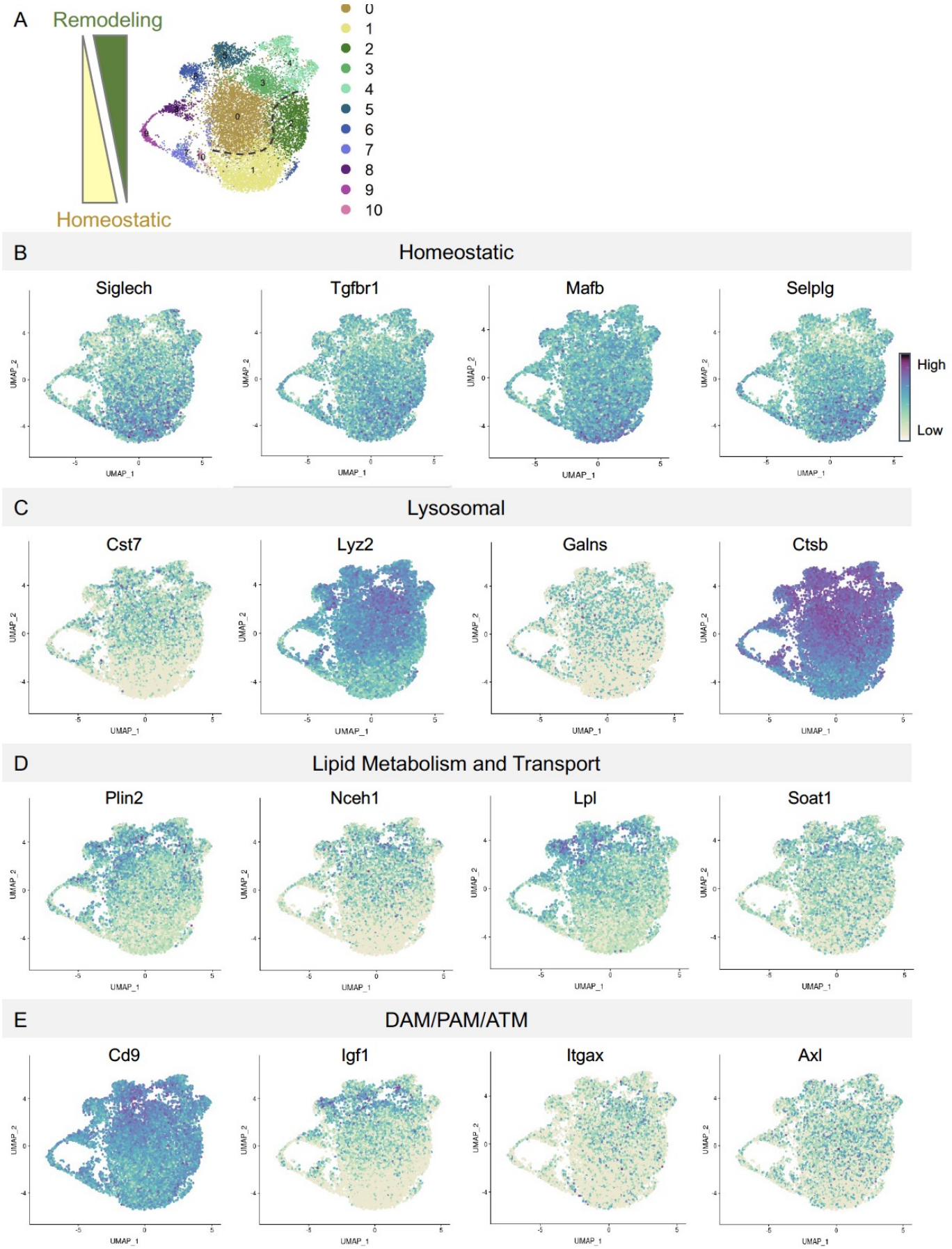

Figure 2. (A) UMAP plot of 11 clusters from all sequenced microglia. Spectrum of homeostatic (bottom) to more remodeling (top). Dashed line demarcates in interface between relatively more homeostatic and remodeling populations. (B) UMAP plots of microglial homeostatic genes. (C) UMAP plots of microglial homeostatic genes important for lysosomal function (D) UMAP plots of genes associated with lipid metabolism. (E) UMAP plots of DAM/PAM/ATM genes. Color scale is based on relative gene expression: dark purple = highest, light yellow = lowest.

3.Neuronal death drives multiple microglial remodeling states

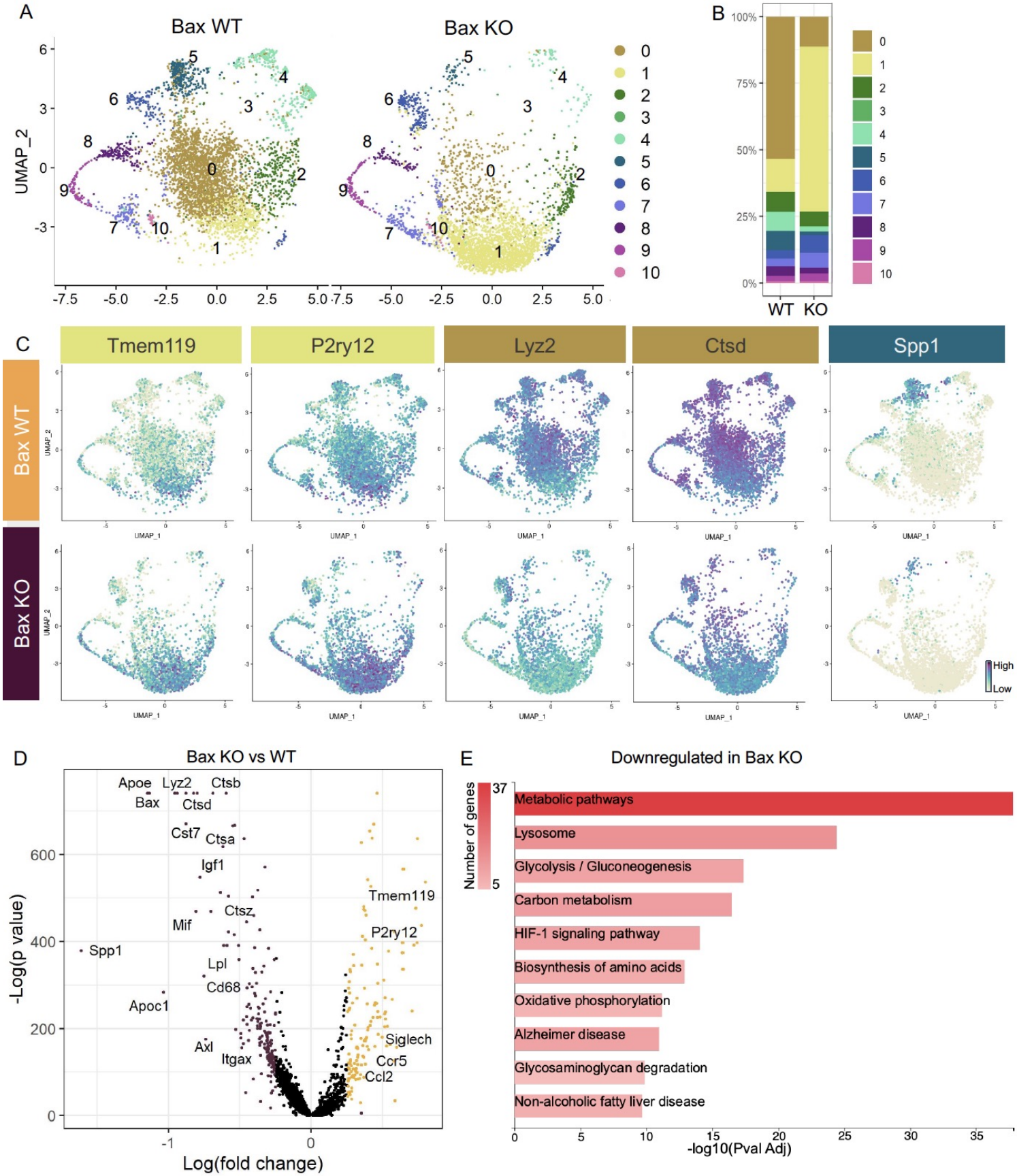

Figure 3. (A) UMAP plot of microglia cells from BAX WT (left) and BAX KO (right) samples distributed into 11 clusters. (B) Bar graph of the proportion of cells in each cluster for each sample. (C) UMAP plots showing expression of representative genes from selected clusters. (D) Volcano plot showing differential gene expression of all BAX KO cells compared to BAX WT cells. Each gene is plotted according to the significance (-Log(p value)) and magnitude (Log(fold change)) of the difference such that those genes enriched in BAX KO have Log(fold change) > 0. Red points indicate genes with p-value ≤0.05 and Log(fold change) > 0.25. (E) KEGG pathway analysis of 183 genes downregulated in BAX KO compared to WT using GeneCodis 4.

Supplemental Fig 7. Bax KO retinas have reduced microglial density

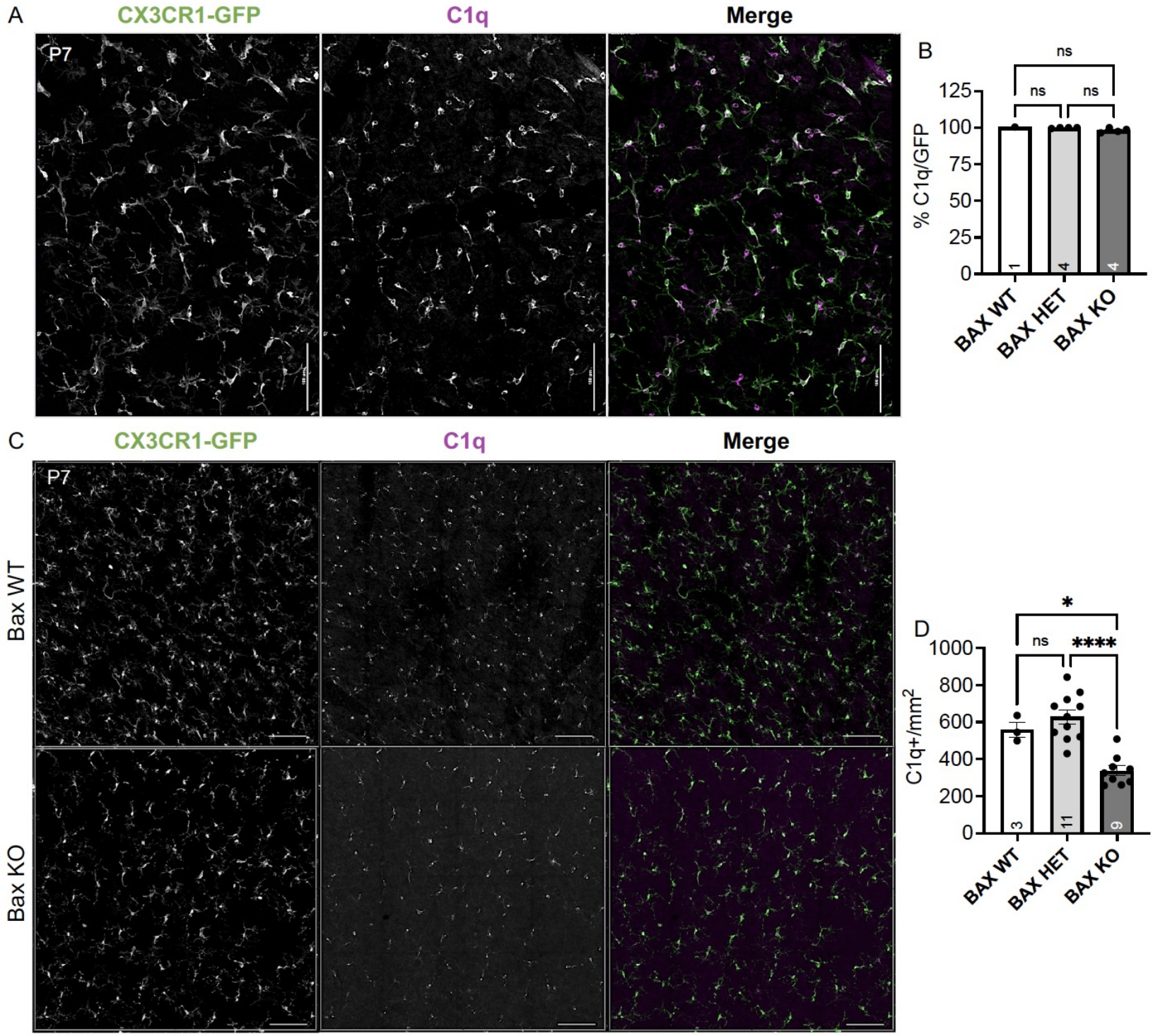

Figure S7. Related to Figure 3. (A) Max projected confocal image of a representative P7 whole mount retinas. CX3CR1-GFP/+ (green); C1q (magenta). Scale bar 100 µm. (B) Percent colocalization of $C1q^+$ cells to CX3CR1-GFP^+. (n=1 WT, n=4 HET, n=4 KO ; ±SEM) Kruskal-Wallis test statistic=4.818, p=0.0667. (C) Max projected confocal image of whole mount immunostained retinas of BAX WT and BAX KO. CX3CR1-gfp (green); C1q (magenta). Scale bar 50 µm. (D) Quantification of $C1q^+$ microglia in a 0.526mm^2 area of the dorsal, mid-peripheral, vascularized region of the retina. (n=3 WT, n=11 Het, n=9 KO; ±SEM) One-way ANOVA F(2,20)=19.90 p<0.0001 and Tukey's multiple comparisons test *p=0.0112, ****p<0.0001.

4. Subsets of remodeling states survive CSF1R inhibition, while homeostatic microglia are more vulnerable

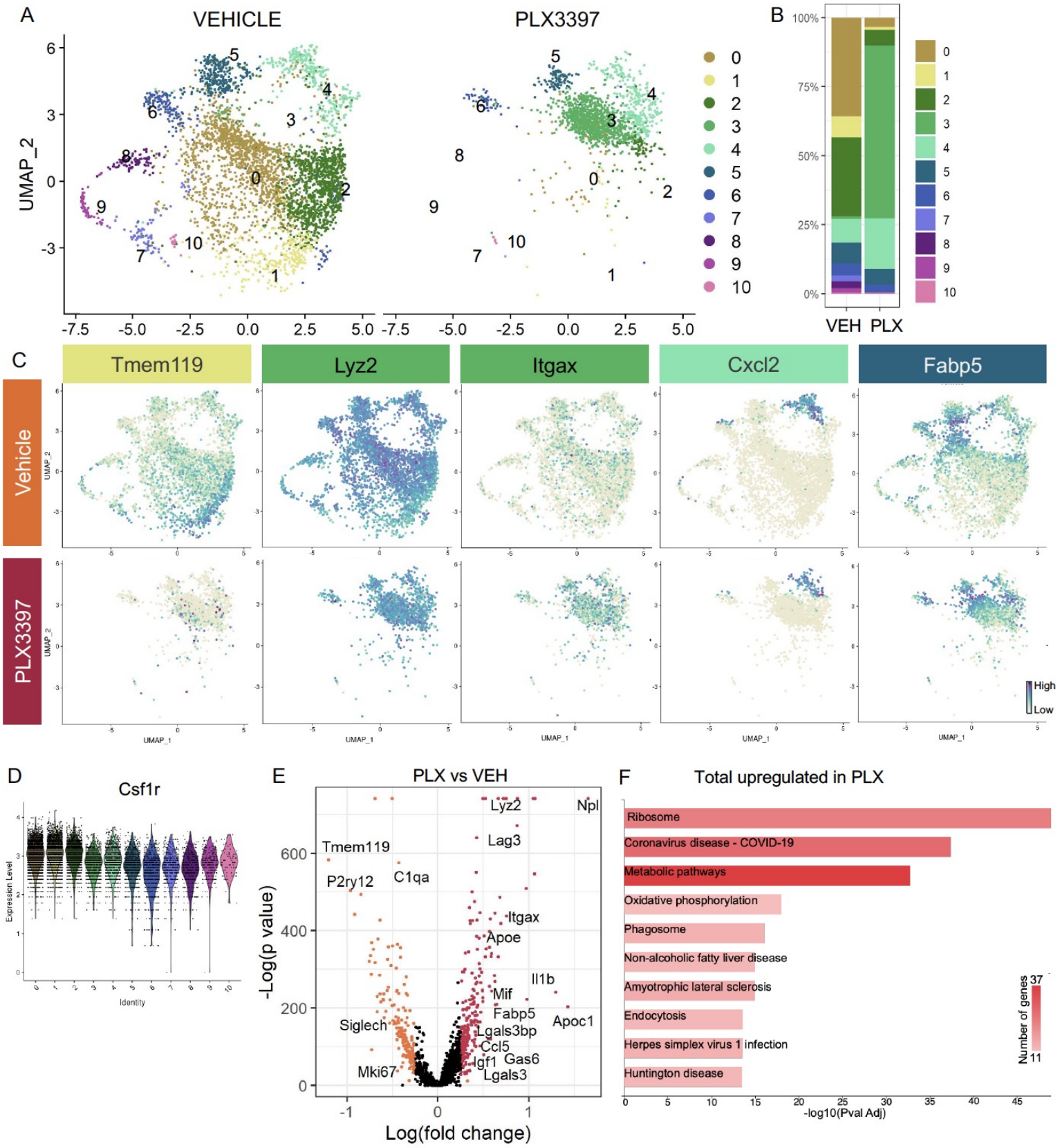

Figure 4. (A) UMAP plot of microglia cells from Vehicle (left) and PLX3397 (right) samples distributed into 11 clusters. (B) Proportion of cells from each sample within each cluster. (C) UMAP plots showing expression of representative genes from selected clusters. (D) Violin plot of Csf1r expression across clusters. (E) Volcano plot showing differential gene expression of pseudobulked PLX cells compared to Vehicle cells. Each gene is plotted according to the significance (-Log(p value)) and magnitude (Log(fold change)) of the difference such that those genes enriched in PLX have Log(fold change) > 0. Red points indicate genes with p-value ≤ 0.05 and Log(fold change) > 0.25. (F) KEGG Pathway analysis of 254 upregulated genes in PLX compared to Vehicle using GeneCodis 4.

5. MerTK and CR3 are required for apoptotic RGC clearance

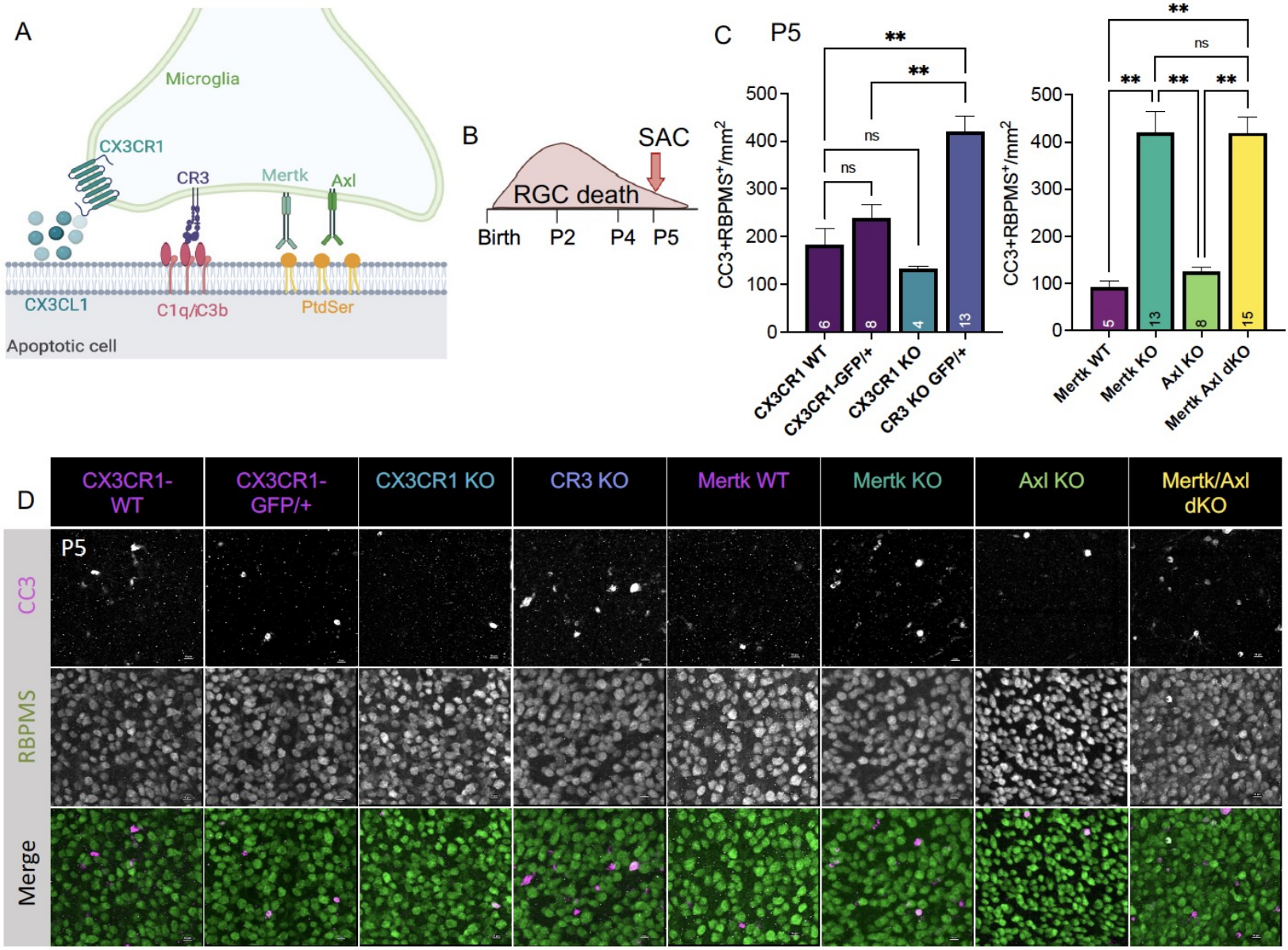

Figure 5. (A) Cartoon schematic of candidate pathways. (B) Schematic for collection at P5 after the bulk of RGC developmental death. (C) Quantification of the average of central and peripheral 0.4 mm^2 RGC death (±SEM) (Figure S9C) in dorsal leaf of all genotypes (n=6 CX3CR1 WT, n=8 CX3CR1-GFP/+, n=4 CX3CR1 KO, n=13 CR3 KO, CX3CR1-GFP/+, n=5 Mertk WT, n=13 Mertk KO, n=8 Axl KO, n=15 Mertk Axl dKO). (left) Welch's ANOVA test W(3,12.58)=23.75, ****p<0.0001 and Dunnett's T3 multiple comparisons test. CX3CR1 WT vs CX3CR1-GFP/+ ns, CX3CR1 WT vs CX3CR1 KO ns, CX3CR1 WT vs CR3 KO **p=0.0016, CX3CR1-GFP/+ vs CX3CR1 KO *p=0.035, CX3CR1-GFP/+ vs CR3 KO **p=0.004, CX3CR1 KO vs CR3 KO ****p<0.0001. (right) Kruskal-Wallis test statistic=25.97 ****p<0.0001 and Dunn's multiple comparisons test. Mertk WT vs Mertk KO **p=0.001, Mertk WT vs Axl KO ns, Mertk WT vs Mertk Axl dKO **p=0.0014, Mertk KO vs Axl KO **p=0.0026, Mertk KO vs Mertk Axl dKO ns, Axl KO vs Mertk Axl dKO **p=0.0036. Not all comparisons shown on graphs. (D) Max projected confocal images of dying RGCs ($CC3^+RBPMS^+$) in KOs in the dorsal mid-periphery in the ganglion cell layer. Apoptotic bodies, CC3 (magenta); RGCs, RBPMS (green). Scale bars 10μm.

Supplemental Fig 8. Loss of candidate receptors does not affect microglial density, RGC density, or BV development

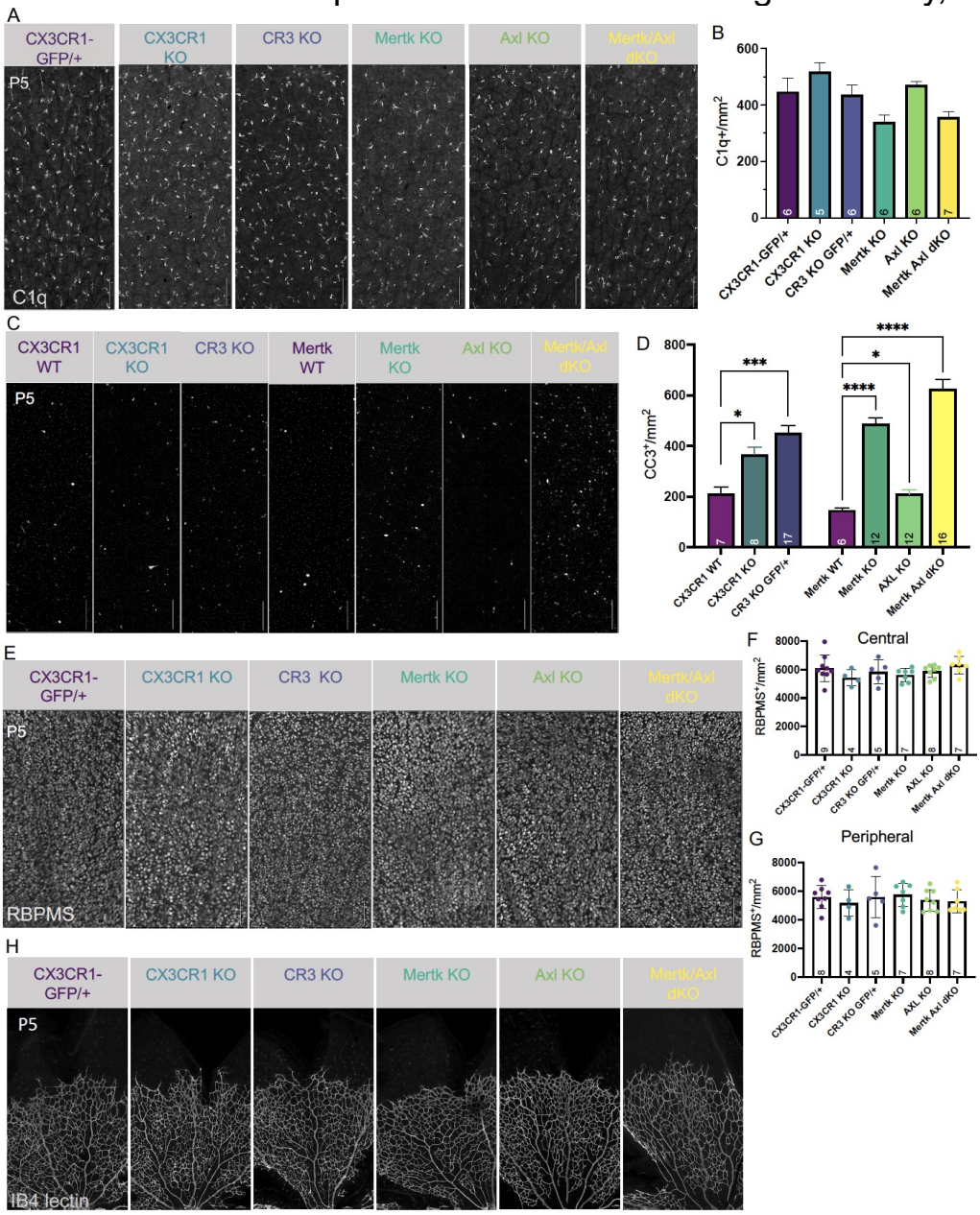

Figure S8. Related to Figure 5. (A) Max projected confocal images of whole mount immunostained retinas of all genotypes at P5 of dorsal leaf, mid-peripheral region. C1q (mono). Scale bar 100µm. (B) Microglia density ($C1q^+/mm^2$) for each genotype in dorsal leaf, mid-peripheral, vascularized region. (n=6 CX3CR1-GFP/+, n=5 CX3CR1 KO, n=6 CR3 KO CX3CR1-GFP/+, n=6 Mertk KO, n=6 Axl KO, n=7 Mertk Axl dKO; ±SEM). Kruskal-Wallis test statistic = 15.91 **p=0.0071 and Dunn's multiple comparisons tests CX3CR1 KO vs Mertk KO *p=0.0489, CX3CR1 KO vs Mertk Axl dKO *p=0.0432, rest of the comparisons, ns. (C) Max projected confocal images of whole mount immunostained retinas of all genotypes at P5 of dorsal leaf, mid-peripheral region. CC3 (mono). Scale bar 100µm. (D) Total apoptotic body density ($CC3^+/mm^2$) for each genotype in entire dorsal leaf (Figure S9A). (n=7 CX3CR1 WT, n=8 CX3CR1 KO, n=17 CR3 KO CX3CR1-GFP/+, n=6 Mertk WT, n=12 Mertk KO, n=12 Axl KO, n=16 Mertk Axl dKO; ±SEM). Welch's ANOVA W(6, 27.82)=54.71 ****p<0.0001 and Dunnett's T3 multiple comparisons test. CX3CR1 WT vs CR3 KO ***p=0.0003, CX3CR1 WT vs CX3CR1 KO *p=0.0328, CX3CR1 WT vs Mertk WT ns, CX3CR1 WT vs Mertk KO ****p<0.0001, CX3CR1 WT vs Axl KO ns, CX3CR1 WT vs Mertk Axl dKO ****p<0.0001, CR3 KO vs CX3CR1 KO ns, CR3 KO vs Mertk WT ****p<0.0001, CR3 KO vs Mertk KO ns, CR3 KO vs Axl KO ****p<0.0001, CR3 KO vs Mertk Axl dKO *p=0.0257, CX3CR1 KO vs Mertk WT ***p=0.0007, CX3CR1 KO vs Mertk KO ns, CX3CR1 KO vs Axl KO *p=0.0089, CX3CR1 KO vs Mertk Axl dKO ***p=0.0004, Mertk WT vs Mertk KO ****p<0.0001, Mertk WT vs Axl KO *p=0.0467, Mertk WT vs Mertk Axl dKO ****p<0.0001, Mertk KO vs Axl KO ****p<0.0001, Mertk KO vs Mertk Axl dKO ns, Axl KO vs Mertk Axl dKO ****p<0.0001. Not all comparisons shown on graph. (E) Max projected confocal images of whole mount immunostained retinas of all genotypes at P5 of dorsal leaf, mid-peripheral region. RBPMS (mono). Scale bar 100µm. (F and G) RBPMS density for each genotype in dorsal leaf, central (F) and peripheral (G). (n=9,8 CX3CR1-GFP/+, n=4 CX3CR1 KO, n=5 CR3 KO CX3CR1-GFP/+, n=7 Mertk KO, n=8 Axl KO, n=7 Mertk Axl dKO; ±SEM). (F) Central: One-way ANOVA F(6,36)=1.251, p=0.3040 and (G) Peripheral: One-way ANOVA F(6,35)=0.4985, p=0.8051. (H) Max projected confocal images of whole mount immunostained retinas of all genotypes at P5 of dorsal leaf. IB4-lectin (mono). Scale bar 100µm.

Supplemental Fig 9. Analysis of CC3+ and CC3+ RBPMS density

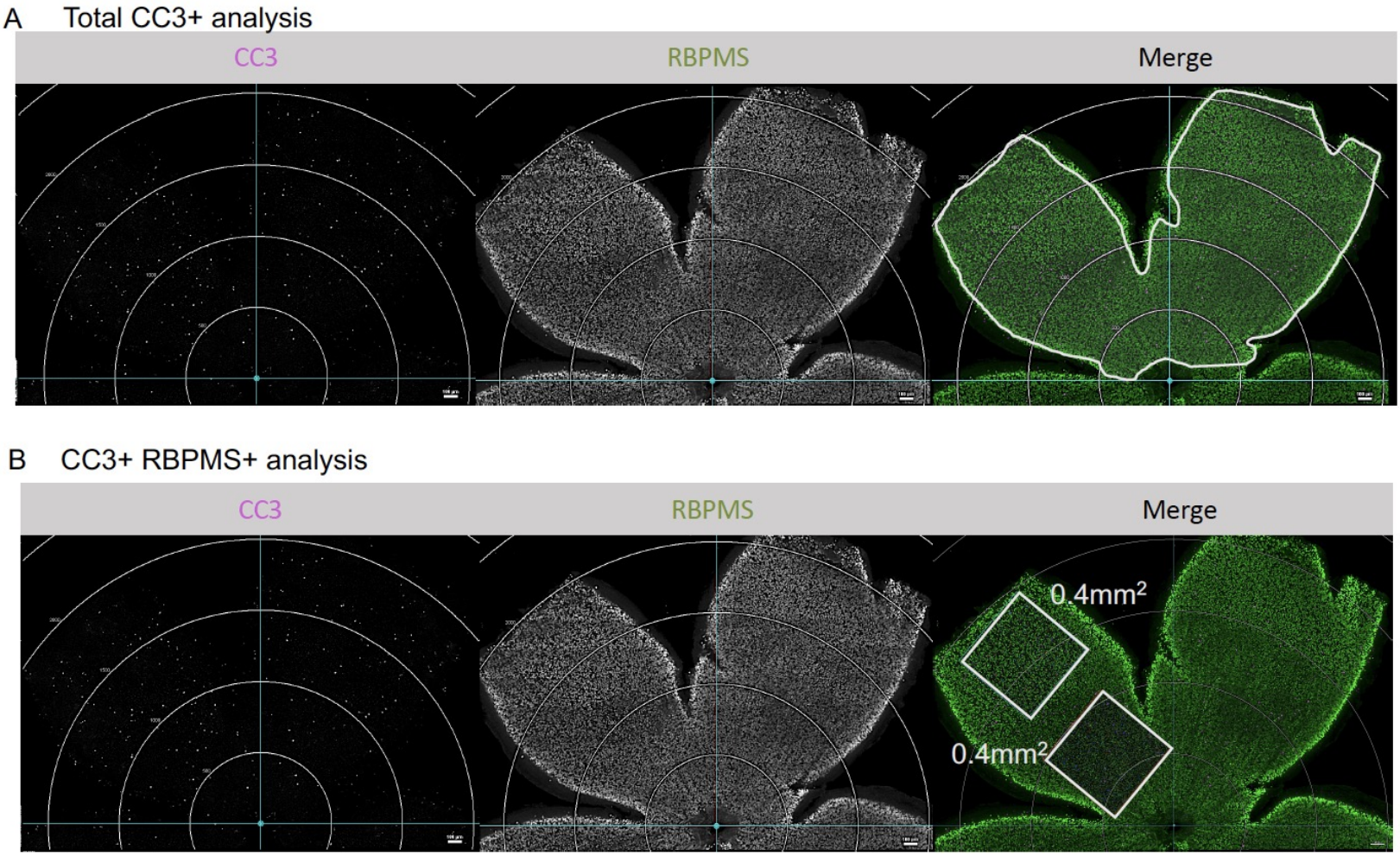

Figure S9. Related to Figure 5 and S8. (A) Max projected confocal images of whole mount immunostained retinas. Apoptotic cells, CC3 (magenta); RGCs, RBPMS (green). Circular grid in increments of 500µm. White line in merge outlines area analyzed for total CC3 analysis. Scale bar 100µm. (B) Confocal of whole mount immunostained retinas. Apoptotic cells, CC3 (magenta); RGCs, RBPMS (green). Circular grid in increments of 500µm. One central and one peripheral ROI of 0.400 mm^2 was analyzed in the dorsal leaf and averaged. Scale bar 100µm.

6. Axl signaling promotes microglial survival in the absence of CSF1R signaling

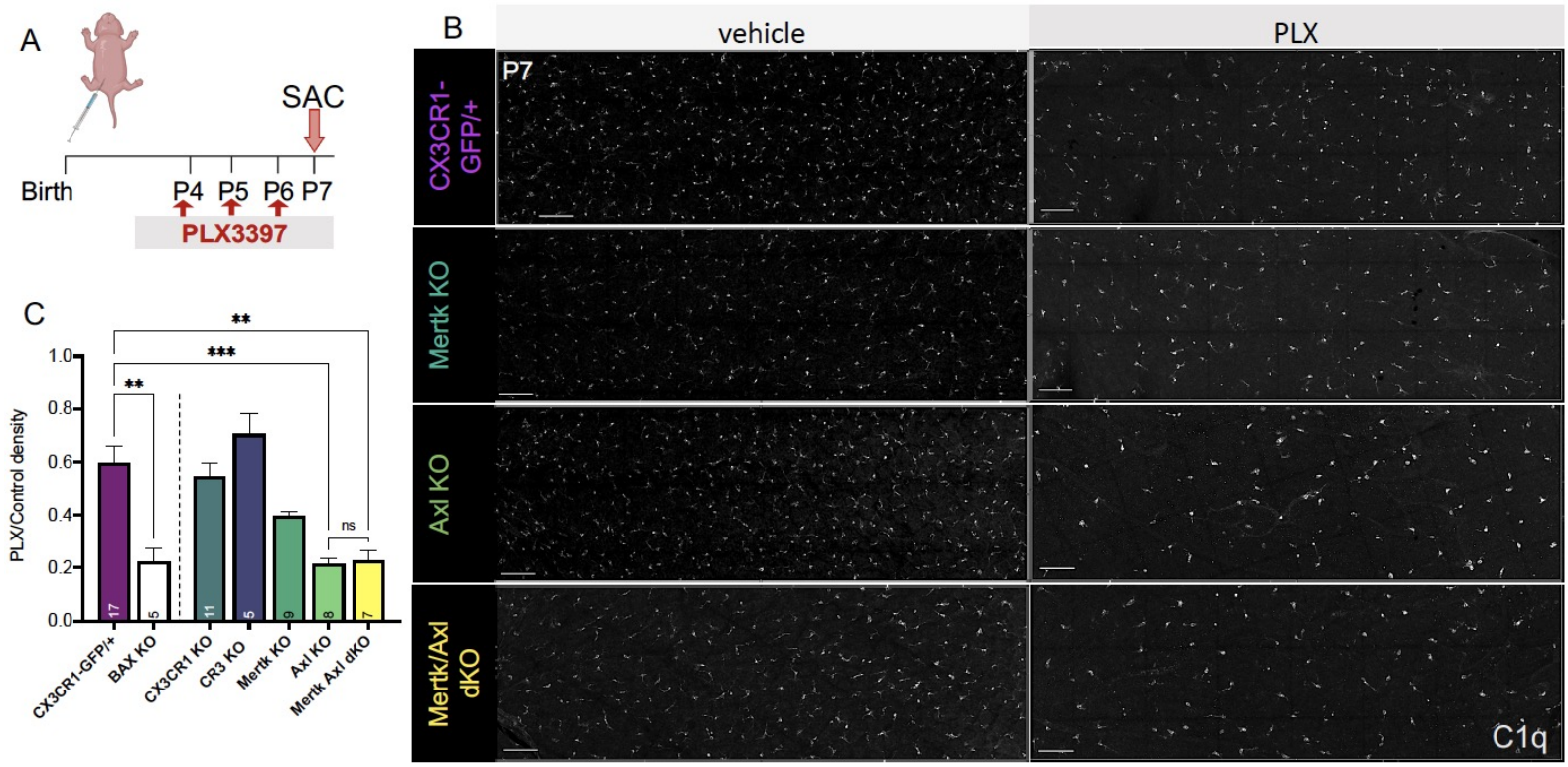

Figure 6. (A) Dosing regimen of PLX3397 to various genotypes. (B) Confocal images of microglia in the NFL/GCL in all genotypes from central to mid-periphery of the dorsal leaf. C1q (mono). Scale bars 100µm. (C) Ratio of density of $CD45^{+}CX3CR1\text{-}gfp^{+}$ or $CD45^{+}CD11b^{+}$ (microglia/singlets) in PLX treated retinas over genotype-matched controls by flow cytometry. CX3CR1-GFP/+ and BAX KO data was previously published [19]. (n=17 CX3CR1-GFP/+, n=5 BAX KO, n=11 CX3CR1 KO, n=5 CR3 KO CX3CR1-GFP/+, n=9 Mertk KO, n=8 Axl KO, n=7 Mertk Axl dKO; ±SEM). Welch's ANOVA W(6,18.55)=16.53, ****p<0.0001 and Dunnett's T3 multiple comparisons test. GFP/+ vs BAX KO **p=0.005, GFP/+ vs CR3 KO ns, GFP/+ vs CX3CR1 KO ns, GFP/+ vs Mertk KO ns, GFP/+ vs AXL KO ***p=0.0004, GFP/+ vs Mertk Axl dKO **p=0.001, BAX KO vs CR3 KO *p=0.0168, BAX KO vs CX3CR1 KO *p=0.0151, BAX KO vs Mertk KO ns, BAX KO vs Axl KO ns, BAX KO vs Mertk Axl dKO ns, CR3 KO vs CX3CR1 KO ns, CR3 KO vs Mertk KO ns, CR3 KO vs AXL KO *p=0.0185, CR3 KO vs Mertk Axl dKO *p=0.0175, CX3CR1 KO vs Mertk KO ns, CX3CR1 KO vs Axl KO ***p=0.0008, CX3CR1 KO vs Mertk Axl dKO **p=0.0021, Mertk KO vs Axl KO ****p<0.0002, Mertk KO vs Mertk Axl dKO *p=0.0394. Axl KO vs Mertk Axl dKO ns. Not all comparisons shown.

7. MerTK and Axl are not required for expression of lysosomal, lipid metabolism, or remodeling genes

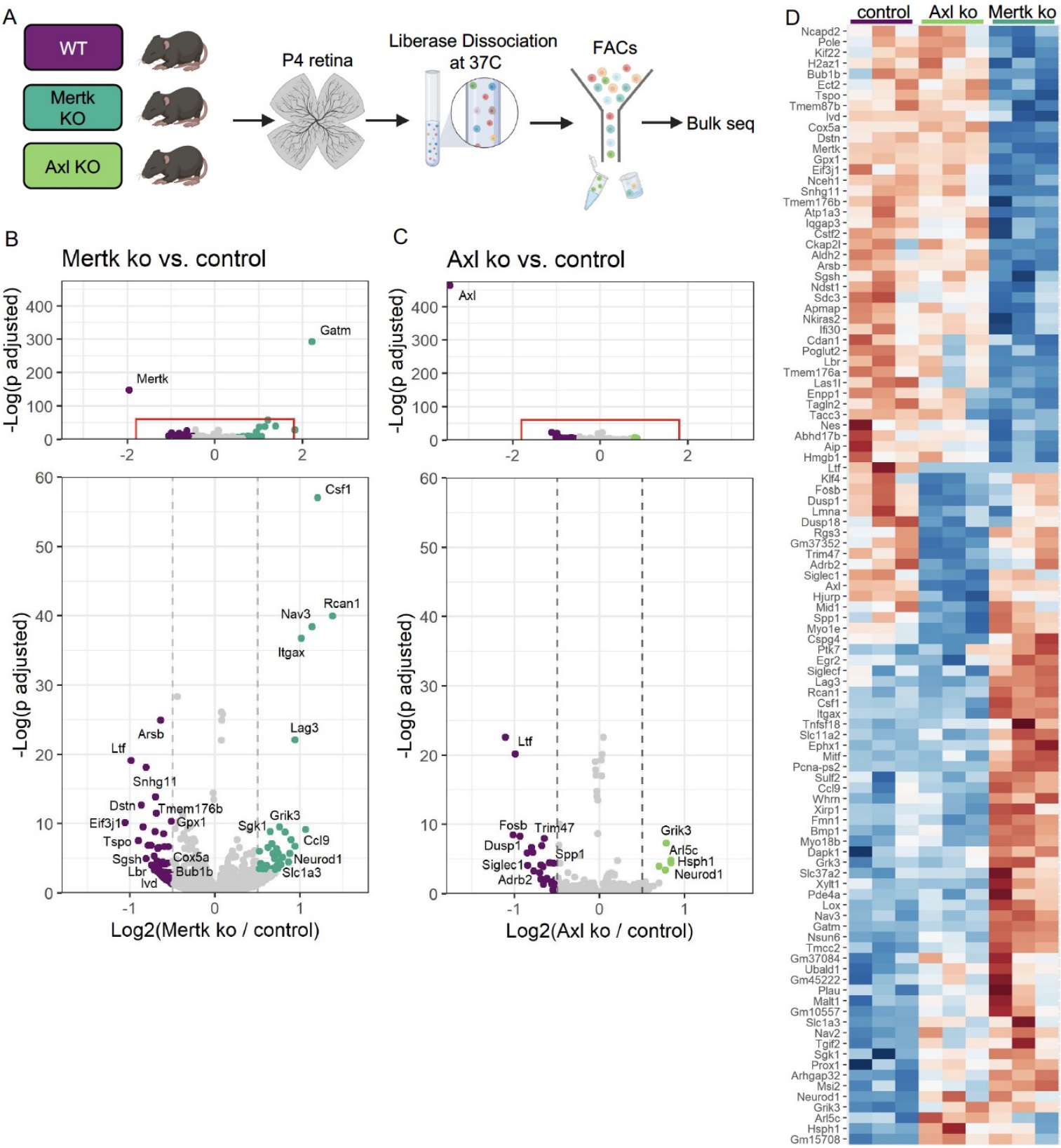

Figure 7. (A) Workflow for P4 retinal collection, dissociation, sorting, and sequencing of individual microglia from 3 different groups: WT, Mertk KO, and Axl KOs (n=3 each). (B,C) Volcano plot of differentially expressed genes. Top: showing all genes and bottom: zoomed in as indicated in red square. Each gene is plotted according to the significance (-Log(p value)) and magnitude (Log(fold change)) of the difference such that those genes enriched in KO have Log(fold change) > 0. Colored points indicate genes with p-value ≤ 0.05 and Log(fold change) > 0.5. (B) Comparison of Mertk KO relative to WT and (C) comparison of Axl KO relative to WT. (D) Heatmap of all differentially expressed genes between WT compared to Mertk KO and WT compared to Axl KO. Color represents z score of normalized gene expression across all samples. Red=high, blue=low.

Supplemental 10. Mertk Axl dKOs do not have substantially altered lysosomal, lipid metabolism, or remodeling gene expression

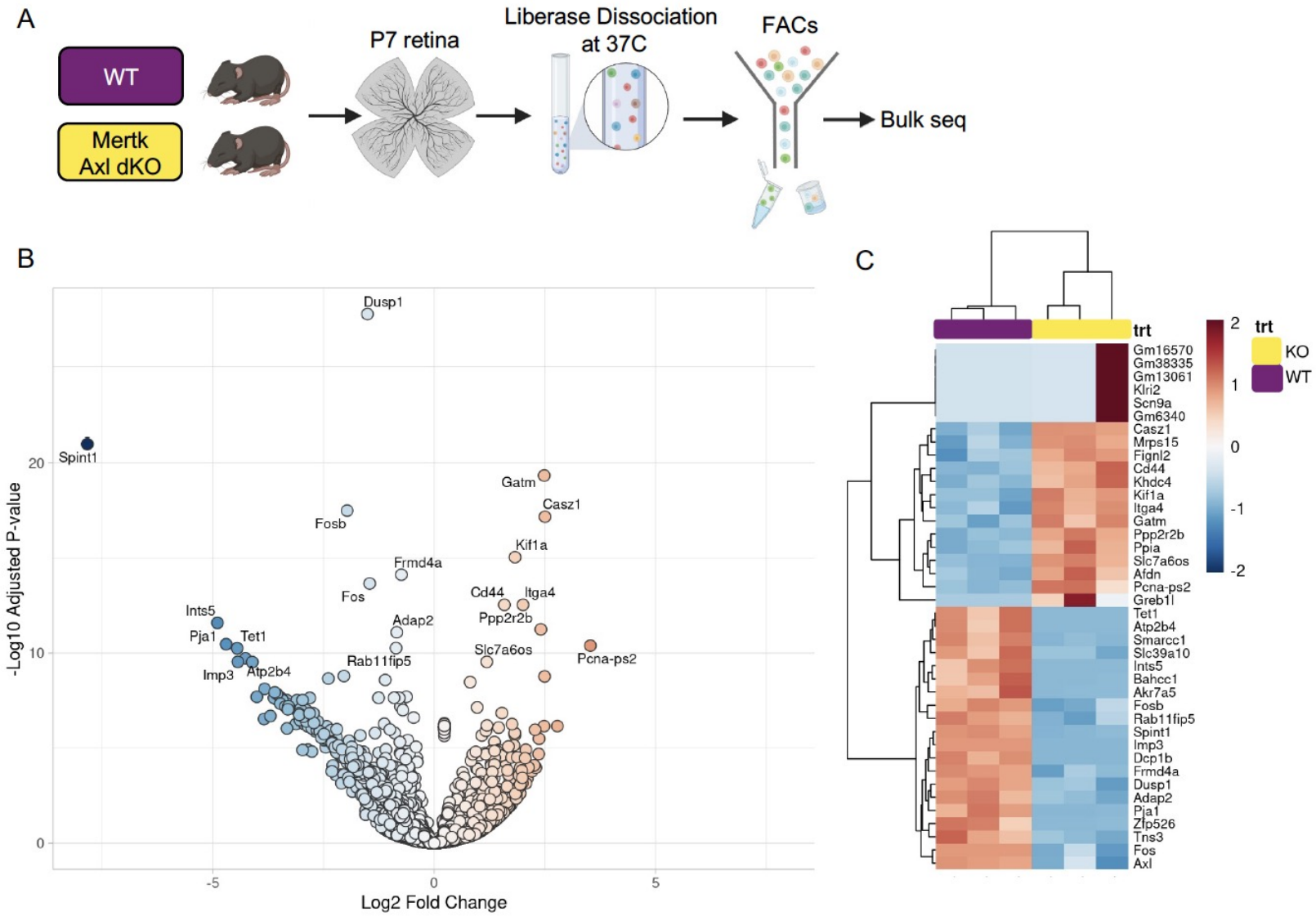

Figure S10. Related to Figure 7. (A) Workflow for P7 retinal collection, dissociation, sorting, and sequencing of individual microglia from 2 groups: WT, Mertk Axl dKO (n=3 each). (B) Volcano plot of differential expression analysis on WT compared to Mertk Axl dKO microglia. 404 upregulated and 1013 downregulated genes in dKO vs WT based on padj <0.05. (B) Heatmap of bulk sequencing on sorted microglia from WT and Mertk Axl dKO retinas top 20 genes upregulated and downregulated in dKO vs WT. Color represents z-score of normalized gene expression across all 6 samples.